Neural coordination mechanisms for associative memory recall and decision making in the hippocampal-prefrontal network

Authors: Claire A. Symanski[1], John H. Bladon[2], Emi T. Kullberg[2] and Shantanu P. Jadhav[1,2,3]*

Affiliations:

[1]Graduate Program in Neuroscience, Brandeis University, Waltham, MA, 02453, USA

[2]Neuroscience Program, Department of Psychology, Volen National Center for Complex Systems, Brandeis University, Waltham, MA, 02453, USA

[3]Lead Contact

*Correspondence to: shantanu@brandeis.edu (S.P.J.)

SUMMARY

Associative memory recall involves brain-wide networks comprising sensory and cognitive regions, with key roles for the hippocampus and prefrontal cortex (PFC). To investigate underlying network coordination mechanisms, we monitored activity in olfactory, hippocampal, and prefrontal regions in rats performing an associative memory task in which they recalled odor-place associations to obtain reward. During recall, the beta rhythm (15-30 Hz) was prominent and coherent across the three regions for correct decisions. Furthermore, single neurons and ensembles in both hippocampus and PFC encoded recalled associations. Ensemble dynamics predicted animals' upcoming decisions and were linked specifically with beta rhythm coordination. Despite this relationship, we found that beta rhythms did not directly phase-modulate all association-coding neurons. Our findings suggest that beta rhythms coordinate ensemble activity within the hippocampal-prefrontal network to support associative memory recall and decision making, and play a permissive rather than instructive role in this process.

KEYWORDS

Hippocampus; Prefrontal cortex; Memory recall; Associative recall; Beta oscillations; Respiratory rhythm, Phase locking; Decision making

HIGHLIGHTS

- Beta rhythms (15-30Hz) coordinate olfactory-hippocampal-prefrontal networks
- Beta coordination supports accurate odor-space associative memory recall
- Single units and ensembles in CA1 and PFC encode associations and upcoming choices
- Beta plays a permissive role in coordinating CA1-PFC ensemble activity underlying recall

INTRODUCTION

The ability to recall associations from memory and use them to guide behavior is a key aspect of cognition across species. Animals can associate sensory cues in the environment with rewarding and noxious outcomes, allowing for adaptive behavior. Associative recall and memory-guided decision making demonstrate the brain's remarkable ability to link familiar cues with actions and beneficial outcomes, but little is known about the mechanisms responsible for these cognitive functions.

Neurons that encode learned associations have been reported in multiple regions in different sensory modalities (Allen et al., 2016; Fitzgerald et al., 2011; Igarashi et al., 2014; McKenzie et al., 2014; Moita et al., 2003; Otto and Eichenbaum, 1992b; Schoenbaum and Eichenbaum, 1995; Wirth et al., 2009; Wirth et al., 2003; Yanike et al., 2004). However, sensory cue-guided recall leading to choices necessarily involves a brain-wide network that links primary sensory areas, the medial temporal lobe, and higher cortical areas involved in decision-making and executive function. Numerous studies have highlighted the significance of the hippocampus and prefrontal cortex (PFC) in cognitive processing related to memory and decision making (Battaglia et al., 2011; Euston et al., 2012; Floresco et al., 1997; Lee and Solivan, 2008; Miller and Cohen, 2001). Both regions are known to encode behaviorally relevant cues and task features (Gothard et al., 1996; Hyman et al., 2012; Wiener et al., 1989; Wirth et al., 2009; Wirth et al., 2003; Yanike et al., 2004), and have been shown to play key roles in memory recall (Fortin et al., 2004; Hasegawa, 2000; Siegle and Wilson, 2014; Wiltgen et al., 2004). Notably, coordinated activity between the hippocampus and PFC, supported by bidirectional anatomical connections (Cenquizca and Swanson, 2007; Delatour and Witter, 2002; Ito et al., 2015), has been shown to be critical for learning and memory-guided behavior (Maharjan et al., 2018; Place et al., 2016; Shin and Jadhav, 2016; Shin et al., 2019; Yu and Frank, 2015; Zielinski et al., 2017). Therefore, we focused on the coordinated interactions between hippocampus and PFC

as a potential key mechanism by which familiar cue associations are recalled and translated into memory-guided decisions.

Several studies have shown that rhythmic network oscillations in the local field potential (LFP) are involved in long-range interactions between the hippocampus and PFC (Benchenane et al., 2011; Buzsaki and Draguhn, 2004; Colgin, 2011; Gordon, 2011; Jones and Wilson, 2005; Shin and Jadhav, 2016). In particular, phase coherence in distinct frequency bands across this network has been suggested as a mechanism for network coordination underlying mnemonic functions. Notably, hippocampal-prefrontal coherence in the theta rhythm (6-12 Hz) plays a role in spatial working memory and acquisition of spatial tasks (Benchenane et al., 2010; Gordon, 2011; Hyman et al., 2010; Jones and Wilson, 2005). However, whether similar mechanisms of coordination between hippocampus and PFC underlie sensory-cued recall and decision making is unclear.

Olfactory memory tasks are ideally suited for studying cued memory recall and decision-making in rodents. Rodents rely heavily on odor cues for navigation and foraging, so odor memories are highly salient and robust (Abraham et al., 2004; Eichenbaum, 1998; Rinberg et al., 2006; Uchida and Mainen, 2003). Previous studies using odor memory tasks have found prominent beta (15-30 Hz) oscillations in olfactory regions and the medial temporal lobe during cue sampling, suggesting that the beta rhythm is a potential mode of communication for olfactory information processing (Frederick et al., 2016; Igarashi et al., 2014; Kay and Beshel, 2010; Rangel et al., 2016; Stopfer et al., 2003). In addition to the beta rhythm, the respiratory rhythm (RR; 7-8 Hz) is also prominent in the hippocampus (Chi et al., 2016; Kay, 2005; Kepecs et al., 2006; Lockmann et al., 2016; Verhagen et al., 2007). However, not much is known about the role of these rhythms in coordinating activity in the hippocampal-prefrontal network. Given the involvement of both the hippocampus and PFC in odor-memory tasks (Alvarez et al., 2002; Eichenbaum et al., 1986; Fujisawa et al., 2008; Fujisawa and Buzsaki, 2011; Martin et al., 2007; Otto and Eichenbaum, 1992a; Peters et al., 2013; Place et al., 2016), and the role of

hippocampal-prefrontal networks in memory retrieval (Churchwell et al., 2010; Fortin et al., 2004; Hasegawa, 2000; Moser and Moser, 1998; Wiltgen et al., 2004; Wiltgen et al., 2010), the representation of recalled odor-cued associations and corresponding rhythmic activity in this network has the potential to shed light on the mechanisms underlying associative recall and memory-guided decision making.

Here, we employed an odor-place association task in which rats were required to recall familiar associations between odor cues and reward locations on a T-maze to elucidate these mechanisms. We found a specific role of beta rhythms in coordinating the olfactory-hippocampal-prefrontal network for accurate memory recall. Beta rhythms played a permissive role in the emergence of hippocampal-prefrontal ensemble dynamics that represented recalled associations and governed animals' upcoming decisions.

RESULTS

Odor-place associative memory recall task

The odor-cued spatial associative memory task required rats to sniff at a nosepoke where one of two possible odors was presented using a calibrated olfactometer (see **STAR Methods**). The rats were required to choose the correct associated reward arm on the T-maze based on the sampled odor identity, where they would receive a reward of evaporated milk (**Figure 1A**).

Rats were habituated to the maze and pre-trained on the task before surgical implant of a microdrive array for recording neural data. Following post-operative recovery and during electrophysiological recording, animals maintained a high level of performance on the task, indicating accurate retrieval of the odor-place association (**Figure 1B**, n = 8 rats, 77.0% ± 1.3%, mean +/- s.e.m.). Rats were required to hold their nose in the nosepoke for a minimum of 0.50

seconds on each trial and were allowed to continue sniffing the odor for any length of time after the minimum threshold was reached. The average odor-sampling duration before nosepoke disengagement was 0.82 ± 0.02 seconds (mean ± s.e.m. across sessions), and this duration was similar between correct and incorrect trials (**Figure 1C**; rank-sum test, $p = 0.12$, distribution shown in **Figure S1A**). The animals' average velocity during the task showed a decrease in speed from the pre-odor to the odor sampling period in the nosepoke, followed by an increase in speed as they left the nosepoke to run to the reward location (**Figure S1B-C**). In two animals, a thermocouple was implanted in the nasal cavity to measure the sniff rhythm (see **STAR Methods**). There was a small but significant increase in sniff rate during the odor sampling period (7.1 ± 0.39 Hz, mean ± s.e.m.) compared to time matched pre-odor periods (6.2 ± 0.29 Hz, mean ± s.e.m.) (**Figure S1D**).

Notably, we observed that on a majority of trials (95.4% ± 0.12%), the animals' turn direction away from the nosepoke matched the direction of the T-maze reward arm that they would ultimately choose on that trial. This behavioral phenomenon was not required for successful performance of the task, and it occurred regardless of whether the trial was correct or incorrect (**Figure 1D**; binomial tests, $p < 0.001$). This observation indicates that the rats recall the odor-place association and choose the reward location for each trial *during* the odor sampling and memory recall period, before exiting the nosepoke to run toward reward, providing a temporal window between with odor onset and nosepoke offset to investigate mechanisms underlying recall.

Beta rhythms specifically underlie odor-space associative memory recall

We therefore focused on the odor sampling period and first sought to determine the network dynamics that underlie coordination of brain regions for memory recall. We used a

tetrode microdrive array to record local field potentials (LFPs) and single units from the dorsal CA1 region of the hippocampus, the prelimbic region of the prefrontal cortex (PFC, primarily prelimbic area), and the olfactory bulb (OB, only LFP) in rats as they performed the odor-place association task (see **STAR Methods**; **Figure S2A-B**). The thermocouple signal and LFP traces from CA1, PFC, and OB from an example trial are shown in **Figure 2A**, along with the same LFP signals filtered in the 15-30 Hz band (additional example shown in **Figure S2C**). We observed a strong increase in power in the beta band (15-30 Hz) during the recall period compared to a time-matched pre-odor period across all three regions (**Figure 2B**; **Figures S2D;** sign-rank tests, $p < 0.01$). Similar increases in beta power during odor discrimination tasks have been reported previously in OB, CA1, and lateral entorhinal cortex (Frederick et al., 2016; Igarashi et al., 2014; Kay and Beshel, 2010; Rangel et al., 2016). The respiratory rhythm (RR, 7-8 Hz) was also prominent in the LFP in all three regions (Chi et al., 2016; Lockmann et al., 2016) showing an increase in power during odor-sampling compared to time-matched pre-odor periods (**Figure 2B; Figure S2E-F**). This rhythm, corresponding to the respiration rate during odor sampling (**Figure S2F**), has previously been shown to be distinct from the hippocampal theta rhythm (6-12 Hz) (Chi et al., 2016; Lockmann et al., 2016) although there is overlap between the two frequency bands. Additionally, we found phase-amplitude coupling between the beta and RR in all three regions, consistent with previous findings (Lockmann et al., 2016) (**Figure S2G)**.

Odor sampling during the memory recall period thus drives prominent increases in the beta and RR rhythms in OB, CA1 and PFC. We next examined LFP coherence and its temporal dynamics in relationship to behavior. The hippocampal-prefrontal (CA1-PFC) network exhibited prominent and consistent coherence at the beta frequency band during odor sampling (Example from one session shown in **Figure 2Ci,** spectrogram across all animals in reduced time window shown in **Figure 2Cii**). This coherence was specific to the odor-sampling period: it significantly

increased compared to time-matched pre-odor periods (**Figure 2Ciii,** sign-rank test, p = 6.7e-6), and diminished shortly after the rat exited the nosepoke (**Figure 2Ci**). Additionally, we observed coherence in the RR band in the CA1-PFC circuit; coherence in this band also increased during odor sampling compared to pre-odor periods (**Figure 2Ciii,** signed-rank test, $p = 0.002$). During running, strong CA1-PFC coherence in the theta band was observed (**Figure S3A**). Finally, beta and RR coherence were also observed between the CA1-OB and PFC-OB regions, with similar temporal dynamics as CA1-PFC beta coherence (**Figure S3B-C**).

We were curious if these beta power dynamics were limited to the odor sampling location on the maze. Indeed, CA1-PFC network beta power and coherence were clearly isolated to the region near the nosepoke (**Figure 2D**). Since hippocampal sharp-wave ripples (SWRs) have been related to memory retrieval in some tasks (Carr et al., 2011; Joo and Frank, 2018; Norman et al., 2019), we also investigated the occurrence of SWRs. SWR events occurred frequently at the two reward locations, as expected (Buzsaki et al., 1983). However, a distinct lack of SWR events at the nosepoke (**Figures 2D** and **2E**; rank-sum test, $p < 0.001$) suggests that SWR replay is unlikely to play a major role in odor-cued associative memory recall.

To establish whether the beta rhythm, the respiratory rhythm, or both were linked to memory recall and task performance, we compared power and coherence in these rhythms between correct and incorrect trials. Beta power in CA1, PFC, and OB was significantly higher on correct compared with incorrect trials, indicating that high beta power in this sensory-cognitive network is associated with correct task performance (**Figure 2F** (top row), bootstrap test; CA1: $p = 0.016$; PFC: $p < 0.001$; OB: $p = 0.005$). In contrast, RR power was unchanged between correct and incorrect trials in all three regions (**Figure 2F** (bottom row), bootstrap test; CA1: $p = 0.47$; PFC: $p = 0.06$; OB: $p = 0.43$). Similarly, CA1-PFC beta coherence was significantly higher on correct trials than incorrect trials, whereas RR coherence was unchanged

(**Figure 2G**, bootstrap test, beta: p = 0.005; RR: p = 0.41). This pattern was true of CA1-OB coherence as well (**Figure S3D**), but not PFC-OB (**Figure S3E**). These results suggest that beta may play a role in coordinating the sensory and cognitive elements of the network to support memory retrieval and decision making, and the RR may play a more passive role in organizing sensory information transfer.

In order to directly examine the influence of rhythmic coordination on task performance dynamics, we next asked whether the animal's decision latency, indicated by nosepoke exit time, was linked to the degree of network coordination. Correlations between the decision latency time and beta/ RR coherence indicated that higher beta coherence between CA1-PFC was significantly correlated with faster decisions, whereas here was no significant correlation between RR coherence and decision latency time (**Figure 2H,** beta: r = -0.11, p = 1.7e-9; RR: r = -0.013, p = 0.47). Similarly, CA1-OB beta coherence, but not RR coherence, was also correlated with decision latency (**Figure S3F-G**). We also confirmed that this elevated beta coherence was specifically seen during odor-cued recall and not during randomly rewarded air trials, whereas RR coherence was similar for odor and air trials (**Figure S3H-J**). Together, these results suggest that the beta rhythm plays a principal role in odor-space associative memory recall and decisions.

Single neurons in CA1 and PFC exhibit association selectivity during odor sampling

In addition to LFP, we recorded single units from hippocampal CA1 (n = 1,309 units) and PFC (n = 717 units) (distribution of neurons across animals shown in **Table S1**). Units that were active during run sessions were categorized into pyramidal cells and interneurons based on firing rate and spike width (see **STAR Methods**). Pyramidal cells were then further categorized as odor-responsive or non-odor responsive based on whether they exhibited significant changes in firing rate during odor sampling (see **STAR Methods**; n = 125 odor-responsive CA1 cells, n =

157 odor-responsive PFC cells). Interestingly, we observed an overall decrease in spiking in the average peri-stimulus time histograms when pooling all spikes from all cells during the odor-sampling period (**Figure S4A**), suggesting a decrease in overall responsiveness in CA1 and PFC networks during odor sampling.

A subset of odor-responsive cells were selective for odor-place association; selectivity was calculated by generating a selectivity index (SI), in which the difference between the average firing rate response to each odor on correct trials was divided by the sum of the two responses, giving a value between -1 and 1 (see **STAR Methods** (Igarashi et al., 2014)). To determine significance, the SI value for each cell was compared to a distribution of SIs generated by shuffling the odor identities across trials (n = 42 CA1 selective cells, n = 49 PFC selective cells) (**Figures 3A** and **3F, S4B**).

Peri-stimulus time histograms and raster plots for two example selective cells for CA1 and PFC are shown in **Figures 3B** and **3G** respectively. Notably, we found that on incorrect trials, selective cells often exhibited responses to the two odors that were opposite to the responses on correct trials. (Examples shown in **Figures 3C** and **3H**). We found that this phenomenon held true across the population of selective cells, such that overall, the SIs on correct trials were anti-correlated with the SIs on incorrect trials (**Figures 3D-E** and **3I-J). Figure S4C** shows interneuron odor selectivity indices and response properties, which were similar to those of pyramidal cells. Note that since there are only two possible choices on the task, the behavioral response on an incorrect trial is identical to that of a correct trial of the opposite odor. The fact that the neural responses on trials with identical behavioral responses are similar indicates that selective cells are not simply coding the odor identity but are instead responsive to the recalled spatial association and the animal's upcoming choice.

Neural ensemble responses emerge gradually during recall and predict the upcoming choice

We next examined how ensemble dynamics underlie the neural representation of associative recall. We considered all cells that were odor-responsive (regardless of the significance of selectivity index) for our ensemble analyses. For the population of odor responsive cells, we found that the distribution of the peak response times in both CA1 and PFC tiled the entire nosepoke time window (**Figure 4A**). Using a population vector (PV) method as described previously (Igarashi et al., 2014), we found that distinct representations for Odor 1 and Odor 2 in the neural population emerged during the memory recall period (**Figure 4B**). Furthermore, this discriminability emerged earlier in the CA1 ensemble than the PFC ensemble (**Figure 4C**, Bootstrap test, $p = 0.006$). We also computed the Z-scored cross-correlation for all CA1-PFC pairs of odor-responsive neurons ($n = 484$ pairs). The distribution of cross- correlation peak times suggested that CA1 cells slightly lead PFC by a mean of 9 ms (**Figure S4G,** illustrative cell pair shown in **Figure S4H**).

We determined the timing of PV divergence on individual trials by comparing the odor-response PVs on each trial to the average PV on trials with the opposite odor. On individual trials, the timing of odor-response PV divergence for both CA1 and PFC ensembles was correlated with the decision latency (trial rasters shown in **Figure 4D**, correlation shown in **Figure 4E**). This implies a temporal link between the emergence of the association in the CA1 and PFC neural populations, and the moment when the animal decides on a behavioral response.

We next asked whether the timing of this neural ensemble discriminability between the two odors was related to rhythmic coordination in the network. Indeed, we found that CA1 PV divergence time on individual trials was anti-correlated with the strength of CA1-PFC beta coherence, such that high CA1-PFC coherence trials had an earlier PV divergence latency;

however, no significant correlation was seen for PFC PV divergence time.(**Figure 4F**, CA1: r = -0.19, p = 1.4e-6, PFC: r = 0.04, p = 0.13). In contrast, we observed no significant correlation between PV divergence time for ensembles in either region with CA1-PFC RR coherence (**Figure 4G**, CA1: r = 0.007, p = 0.85, PFC: r = -0.009, p = 0.78).

To determine whether the animal's upcoming behavior could be predicted by neural ensembles before the decision was made, we trained a generalized linear model (GLM) to predict the animal's choice based on ensemble activity during the recall period. Reward choice could be accurately predicted starting at least 0.6 seconds after odor onset for CA1 and 0.7 seconds after odor onset for PFC ensembles (**Figure 4H**). These results confirm that the animals recall the odor-place association in the nosepoke and make a choice during this moment, and that beta coordination in the CA1-PFC network supports neural activity dynamics underlying the recall and memory-guided decision making process.

Recall period activity is distinct from spatial activity

We next investigated if there was any relationship between the recall period activity of CA1 and PFC ensembles during odor sampling, and their spatial activity on the maze as the animals ran through the central and side arms toward reward. We examined units from sessions in which animals traversed a long track (see **STAR Methods**, 26 sessions from 6 rats) in order to assess spatial firing characteristics. A large fraction of cells in CA1 and PFC exhibited spatial activity on the maze (see **STAR Methods** for details on spatial parameters, n = 344/585 CA1 cells; n = 159/288 PFC cells had fields on the track), including units that were both odor-responsive (association selective and non-selective) and non-odor-responsive (**Figures 5A, 5B**; examples of CA1 and PFC association-selective cells with spatial fields in **Figure 5A,** examples of CA1 and PFC odor responsive but non-selective cells with spatial fields shown in **Figure S5A**).

Cells that were odor-responsive were more likely to have spatial fields on the track (odor sampling periods were excluded in spatial responses, see **STAR Methods**), compared to cells that were not responsive during the recall period (**Figure 5B**, Binomial test, CA1: p(spatial field)$_{null}$ = 0.57 (n = 273/477), p(spatial field | odor responsive)= 0.66 (n = 71/108), p=0.029; PFC: p(spatial field)$_{null}$ = 0.48 (n = 76/160), p(spatial field | odor responsive) = 0.65 (n = 83/128), p=2.7e-5). Additionally, for both CA1 and PFC neurons, we found that the firing rate during odor sampling was correlated with firing rate during running (**Figure 5C,** CA1: r = 0.39, p = 3.0e-37; PFC: r = 0.68, p = 1.2e-62), and odor-responsive cells had higher firing rates overall (**Figure S5B** rank-sum tests, CA1: p = 2.8e-14; PFC: p = 1.3e-5), suggesting a denser representation of space in this population. To test this, we also examined whether the spatial fields in either CA1 or PFC exhibited different characteristics based on responses during odor sampling. Surprisingly, we found no difference in field width (**Figure 5D,** rank-sum tests, CA1: p = 0.15; PFC: p = 0.92), field peak rate (**Figure S5C**), or field sparsity (**Figure S5D**) between cells that were odor unresponsive and odor responsive in either region.

In addition, we also examined trajectory selectivity as animals ran through the spatial delay period in the central arm and on the side arms toward reward (examples of trajectory selective firing shown in **Figure 5A,** second row). Interestingly, although trajectory-selective cells were significantly more likely than non-trajectory-selective cells to respond to the odors (**Figure S5E**), they were no more association-selective during the recall period (**Figure 5E**, rank-sum tests, CA1: p = 0.74; PFC: p = 0.54). Furthermore, association-selective units were no more likely to fire during the matching run trajectory than the mismatched trajectory (**Figure 5F,** Rank sum test CA1: p = 0.26; PFC: p = 0.20)**.** Thus, although CA1 and PFC cells responsive during the recall period had higher firing rates and therefore higher engagement while traversing trajectories on the maze, there was no clear relationship between association selectivity and trajectory selectivity in either CA1 or PFC.

We then sought to determine whether association selective neuronal activity in the population during recall persisted into the following run period. To examine this, the linearized T-maze was divided into 5 equally spaced quintiles and a Bayesian Classifier trained on odor period activity was used to decode the choice identity from the ensemble activity during run at each spatial quintile (see **STAR Methods**; similar results were seen for spatial quartiles). We found that choice identity could be decoded at the first quintile of track, nearest to the nosepoke, but decoding accuracy diminished to chance level thereafter (**Figure 5G**). In contrast, using spatially active ensembles in the respective spatial quintile as the training set, the animal's upcoming behavioral choice could be accurately decoded at all periods along the trajectory (**Figure 5H**). This suggests that the association selectivity that emerges in ensembles during odor sampling (**Figure 4**) persists transiently for a short period past the nosepoke offset, but that separate ensembles maintain choice-related information as animals traverse the spatial trajectory, corresponding to theta oscillations during run (**Figure 2**). These results together suggest that the association selective ensembles during recall period transiently encode choice during the initial track period, but this shifts to distinct ensembles that maintain choice selectivity during the working-memory period associated with a spatial delay.

CA1 and PFC cells phase lock to beta and respiratory rhythms

Finally, we asked if there was any relationship between oscillatory phase modulation of cells during the recall period and their choice selectivity. Within the population of odor-responsive cells in both CA1 and PFC we found a fraction of cells that were phase locked to the beta rhythm during recall (see **STAR Methods**; CA1: n = 36, 28.8%; PFC: n = 17, 10.8%). Spike-phase histograms for two beta-phase locked cells are shown in **Figure 6A** (Rayleigh Z test, CA1: $z = 4.43$, $p = 0.011$; PFC: $z = 3.12$, $p = 0.04$). For odor-responsive CA1 cells, there

was a significant non-uniformity in beta phase-preference of cells across the population. This trend was not true of odor-responsive PFC cells, however (**Figure 6B-C**, Rayleigh Z test; CA1: z =7.88, p = 3.4e-4; PFC: z = 0.91, p = 0.09).

We also found that many cells in the odor-responsive populations were strongly phase locked to RR (CA1: n = 112, 89.6%; PFC: n = 60, 38.2%). Examples for two of these cells are shown in **Figure 6D** (Rayleigh Z test; CA1: z = 135.3, p = 6.32e-62; PFC: z = 73.9, p = 3.8e-37). Similar to beta phase locking, we found that in CA1 there was a significant non-uniformity in RR phase-preference of cells across the population, but this was not true for PFC cells (**Figure 6E-F**, Rayleigh Z test; CA1: z = 8.83, p = 1.27e-4; PFC: z = 1.39, p = 0.24).

We next asked whether phase locking to the beta rhythm was indicative of accurate memory recall, so we compared Rayleigh Z scores, a measure of non-uniformity in the spike-phase distribution, on correct versus incorrect trials for significantly phase-locked cells. We found that CA1 cells that were phase-locked to the local beta rhythm exhibited a lower Rayleigh Z on incorrect trials. This suggests that spiking modulation by the beta rhythm in CA1 supports retrieval of correct odor-place associations. There was no significant effect for PFC, however, possibly due to the small fraction of beta phase-locked cells (**Figure 6G**, signed-rank test, CA1: p = 0.002, PFC: p = 0.38). We found no change in modulation strength for either CA1 or PFC RR phase-locked cells between correct and incorrect trials (**Figure 6H**, signed-rank test, CA1: p = 0.37, PFC: p = 0.24). These results further support the hypothesis that the beta rhythm is involved in coordinating neural activity for memory recall, and not RR. Note that we found beta phase locking in CA1 to be related to task performance, even though a higher percentage of cells in both regions were phase locked to RR (**Figure 6I**, z-test for proportions, CA1: p = 6.8e-23; PFC: p = 8.8e-9) and CA1 cells were much more strongly phase modulated by RR (**Figure 6J**, rank-sum test; CA1: p = 1.5e-26; PFC: p = 0.17).

Are cells that are modulated by beta the same population of cells that code for the recalled odor association? To test this, we compared the number of cells that were both association-selective *and* phase-locked (within and across regions) to the fraction of cells that would be expected by chance, given the total percentages of cells that are association-selective or phase-locked. Interestingly, we found that the number of cells that fell into this category was no different than chance for either PFC or CA1 (**Figure 6K**, binomial tests; CA1: $p = 0.097$; PFC: $p = 0.17$). We found similar results for RR modulation (**Figure 6L,** binomial tests; CA1: $p = 0.077$; PFC: $p = 0.10$). It should be noted that since such a large majority (~90%) of neurons in CA1 were significantly phase locked to RR, it is unsurprising that almost all the association-selective cells were phase locked to this rhythm. However, this result indicates that the association-selective cells were no more or less likely than non-selective cells to phase lock to RR. These results suggest that, surprisingly, the neural ensembles that code for the primary task parameter of odor-space association are not driven directly by the beta rhythm, despite the relationship of beta to associative recall (**Figures 2, 4**). Rather, we find that beta plays a permissive role by enabling ensemble neural dynamics that underlie recall and decision making (**Figure 4**) in the broader CA1-PFC network.

DISCUSSION

Our results provide new insight into the mechanisms of rhythmic coordination of hippocampal–prefrontal ensembles by beta rhythms for odor-cued recall and memory-guided decision making. We found that during odor-place associative recall, the beta rhythm governs physiological coordination between the olfactory bulb, hippocampus, and PFC for associative recall and decision making. Odor-responsive single unit and ensemble activity in the CA1-PFC network discriminates between the two associations and can reliably predict upcoming behavior. During recall, CA1-PFC ensemble dynamics and beta coherence are linked to decision-making

accuracy and latency. Despite this link, we found no evidence for specific beta phase modulation of association-encoding neurons. Instead, our results suggest that beta oscillations play a permissive role in enabling temporal evolution of ensemble dynamics in the CA1-PFC network for recall and decision making, delineating a novel mechanism by which rhythmic coordination supports cognition.

The mechanisms underlying encoding and recall of associations between sensory cues in the environment are of fundamental interest. Sensory cue-elicited recall and decisions during goal-directed behavior involves widespread networks encompassing sensory regions, medial temporal memory regions, and prefrontal decision-making regions. Prominent odor-driven oscillations have been described in these areas (Chi et al., 2016; Frederick et al., 2016; Igarashi et al., 2014; Kay and Beshel, 2010; Kepecs et al., 2006; Lockmann et al., 2016; Rangel et al., 2016; Stopfer et al., 2003; Tort et al., 2009), which can potentially coordinate these long-range networks.

Here, we used an odor-cued T-maze task to examine which rhythms enable coordination of olfactory-hippocampal-prefrontal networks, and whether these rhythms play a role in patterning ensemble activity in hippocampal-prefrontal network to enable memory recall and decision making. In our task, animals chose a turn direction indicative of their eventual decision on the T-maze immediately after odor sampling, providing a temporal window for cued recall and decision latency from the onset to exit from the odor port. We found increases in power and coherence of both beta (~15-30 Hz) and RR (~7-8 Hz) across the olfactory-hippocampal-prefrontal network during this recall period. However, beta oscillations, and not RR, were correlated with correct performance and decision latency. Further, high beta coherence was specific to odor-cued trials whereas RR coherence remained unchanged between odor-cued and un-cued air trials. Based on this finding, we speculate that encountering a familiar odor

stimulus, rather than sniffing alone, elicits the engagement of the hippocampal-prefrontal network by the beta rhythm.

Interestingly, although hippocampal SWRs have been linked to internal recall and planning (Buzsáki, 2015; Carr et al., 2011; Joo and Frank, 2018), there was very low prevalence of hippocampal SWRs during odor sampling, suggesting SWRs are not directly involved in odor-cued memory retrieval. Instead, our results indicate that beta plays a key role in coordinating hippocampal-prefrontal networks for recall and memory-guided decision making, in addition to coordinating entorhinal-hippocampal networks for odor-cued recall as described previously (Igarashi et al., 2014). It is important to point out that we found a similar range for beta oscillations, 15-30 Hz, as previous studies (Igarashi et al., 2014; Martin et al., 2007). Odor-driven gamma rhythms at 40-100 Hz have also been reported (Beshel et al., 2007; Frederick et al., 2016), and may play complementary roles with beta oscillations in odor-memory tasks, perhaps engaging additional networks for odor processing. We speculate that sensory modality-specific rhythms may play a general role in cue-driven recall by coordinating sensory and cognitive areas, which can be tested in future studies.

Our analysis of single units in the hippocampus and prefrontal cortex revealed a group of cells that were selective for one odor over the other, similar to previous reports in the hippocampus (Eichenbaum et al., 1987; Igarashi et al., 2014). However, we found that these selective cells often exhibited “opposite” selectivity on incorrect trials compared to correct trials, indicating that these cells do not respond solely to the perceptual qualities of the odor, in which case the response would be similar on all presentations of a particular odor regardless of the trial outcome. Instead, this response suggests conjunctive coding of the association between the odor and the upcoming spatial choice, resembling findings from studies of combined cue modalities and cue-context associations (Allen et al., 2016; Ferbinteanu et al., 2011; Fitzgerald et al., 2011; Komorowski et al., 2009; McKenzie et al., 2014; Otto and Eichenbaum, 1992b;

Schoenbaum and Eichenbaum, 1995; Terada et al., 2017). Thus, the CA1-PFC neural response during odor sampling corresponds to recall of the odor-place memory. The sniffing frequency and strength was unchanged between correct and incorrect trials, as indicated similar respiratory rhythms on incorrect trials. Therefore, incorrect trials were unlikely to be caused by inadequate odor sampling, but rather erroneous recollection of the odor association, corresponding to the change in selectivity of the association encoding cells. Future studies that combine recording from the olfactory system together with hippocampus and PFC can potentially unveil how the cue representation evolves from odor perception to the recall-based decision.

We also found that beta rhythms govern temporal evolution of coordinated hippocampal-prefrontal ensemble activity leading to memory recall and decision making. Odor-responsive neural populations exhibited differential activity patterns in response to the two odor-associations during recall, and the animal's upcoming choice could then be predicted from this ensemble activity. Correlation between the timing of ensemble odor discrimination and choice execution indicates that the emergence of the neuronal representation coincides with the cognitive decision. This emergence of neural ensembles that reflect recalled associations may be indicative of a physiological mechanism for dynamic reactivation of memory engrams upon re-encountering the familiar odor stimuli (DeNardo et al., 2019; Liu et al., 2012). Finally, we found a link between the strength of beta coherence, the timing of ensemble discrimination, and the behavioral decision latency. Together, these results signify that rather than an instantaneous moment of recall by memory encoding ensembles, beta rhythms coordinate gradual emergence of CA1-PFC neural ensemble dynamics that underlie recall of stored associations and subsequent decision making.

Interestingly ensemble selectivity emerged earlier in CA1 than PFC and was significantly correlated with CA1-OB beta coherence. We therefore speculate that beta coherence leads to

associative recall initially in hippocampal networks, which subsequently support emergence of choice selectivity in PFC through beta coherence, driving the eventual decision. It remains unclear how these neural dynamics and their relationship to the beta rhythm evolve as animals learn new associations. One possibility is that they resemble the dynamics observed in the hippocampal-entorhinal circuit, in which coordination of the network at the beta rhythm and odor-selective neural activity emerge gradually as animals learn (Igarashi et al., 2014). This can be investigated by examining network dynamics during novel odor-place learning.

It is also noteworthy that we observed different mechanisms underlying associative memory recall and maintenance. Odor-driven beta coherence leads to emergence of ensemble selectivity during the recall period, which is predictive of the animal's upcoming decision, but these ensembles maintain association selectivity only transiently as animals embark on the spatial trajectory toward reward. This selective coding is not maintained by the same ensembles during running, but instead other spatially modulated cells in CA1 and PFC maintain choice coding throughout the track, including the spatial delay period activity. Thus, beta-driven ensembles mediate recall in the hippocampal-prefrontal network, and choice selective activity is then subsequently maintained by theta-driven spatially modulated activity, similar to reports in spatial working memory tasks (Colgin, 2011; Gordon, 2011; Hyman et al., 2010; Jones and Wilson, 2005; O'Neill et al., 2013).

The temporal evolution of ensemble activity underlying recall and decision making, and its relationship to beta oscillations, is reminiscent of temporal coding of odor stimuli mediated by oscillations in the olfactory system (Kepecs et al., 2006; Stopfer et al., 2003). Previous findings indicate that spike timing modulation according to the phase of prominent network rhythms could organize task-encoding neural ensembles to support memory guided behavior and decision-making (Benchenane et al., 2010; Buschman et al., 2012; Papale et al., 2016; Terada et al., 2017; Wikenheiser and Redish, 2015; Zielinski et al., 2019). Therefore, we hypothesized

that units that encoded odor identity and association would be directly modulated by the beta rhythm. Interestingly however, we found that although the strength of beta phase-locking was linked to correct decisions, neurons that encoded the odors were no more likely to be phase-locked to beta than chance level. Notably, phase locking was stronger and more prevalent for RR compared to the beta rhythm, but behavioral performance and decision-related neural activity was linked specifically to the beta rhythm. Our results thus suggest that the beta rhythms play a permissive rather than instructive role in associative recall; instead of direct phase modulation of association coding cells, beta oscillations establish communication and organization of activity in sensory and cognitive networks enabling memory recall and decision making. These results suggest that the observation of neural activity that is phase-locked to a prominent network rhythm need not necessarily be interpreted as encoding of task-relevant features. Rather, oscillatory phase-locking may be indicative of a general network state that enables coordination.

ACKNOWLEDGMENTS

This work was supported by NIH Grant R01MH120228, a Whitehall Foundation award, and a Smith Foundation Odyssey award to S.P.J. We thank the late Howard Eichenbaum for assistance with the behavioral task.

AUTHOR CONTRIBUTIONS

S.P.J. conceived and designed the study, C.A.S. performed experiments and analyzed the data, J.B. analyzed the data, E.K. contributed to experiments, S.P.J. and C.A.S. wrote the manuscript with input from all authors.

DECLARATION OF INTERESTS:

The authors declare no competing interests.

FIGURE LEGENDS

Figure 1: Odor–space associative memory recall task

A. Schematic of odor-cued T-maze task. Odors 1 (heptanol) and 2 (ethyl butyrate) were delivered at the nosepoke in pseudo-random order. Presentation of odors 1 and 2 was associated with milk reward at Reward Locations 1 and 2, respectively. Animals had to recall odor–space associations on each trial and make a choice to visit the correct reward location.

B. Performance of each animal (*n* = 8) on the odor-cued T-maze task (animals 1 - 5) or truncated odor-cued task (animals 6 - 8; truncated task, left-right choice without spatial delay period) across multiple sessions (grey dots). Animal average is indicated by black bars. Dashed line indicates chance level.

C. Nosepoke duration across all animals for correct trials (n = 3174) and incorrect trials (n = 1008). Boxplots indicate interquartile range. (rank-sum test, $p = 0.12$).

D. Turn direction away from nosepoke in relation to chosen reward well. Pie charts indicate the fraction of trials in which, at the nosepoke, animals turned in the same direction versus the opposite direction as the reward well that they would ultimately choose. Sessions in which animals ran the truncated task without spatial delay period were excluded. (correct trials: n = 1624 same direction, 32 opposite direction, binomial test, $p < 0.001$. incorrect trials: n = 499 same direction, 21 opposite direction, $p < 0.001$).

Figure 2: Beta rhythms specifically underlie coordination for odor–space associative memory recall

A. Examples of responses to odor from one trial. Top to bottom: Respiratory rhythm recorded via thermocouple, raw LFP signal in CA1 from a single tetrode, the same CA1 signal filtered in the beta band (15-30 Hz), raw LFP signal in PFC from a single tetrode, the same PFC signal filtered in the beta band, raw LFP signal in OB from a single tetrode, and the same OB signal filtered in the beta band. Area between dashed lines indicates odor sampling period.

B. Time-frequency plots showing power spectra across all animals and tetrodes aligned to odor onset. Color scale represents z-scored power for each region: Thermocouple (signal from n = 2 animals, max 0.92; min -0.30), CA1 (n = 97 tetrodes, max 0.29; min -0.33), PFC (n = 105 tetrodes, bottom; max 0.58; min -0.15), and OB (n = 11 tetrodes, max 2.28; min -0.20). Area between vertical dashed lines indicates odor sampling period. Beta band is marked by blue bracket, and RR band is marked by pink/red? bracket.

C. CA1-PFC coherence spectra. Color scale represents z-scored coherence.

   i. CA1-PFC coherence for a single animal during the full task time window starting from odor sampling (area between vertical dashed lines) to reward (vertical solid line indicates reward onset). Coherence is averaged across all inter-regional tetrode pairs. (n = 58 tetrode pairs, max 0.79; min -0.45).

   ii. Coherence across all animals and all tetrode pairs (n = 582 tetrode pairs, max 0.51; min -0.34). Beta band is marked by blue bracket (15-30 Hz). RR band is marked by pink bracket (7-8 Hz). Dashed line indicates average odor-offset.

   iii. Coherence during odor periods and time-matched pre-odor periods, across all tetrode pairs. Error bars indicate s.e.m. Left: beta coherence (signed-rank test, p = 6.7e-6***).Right: RR coherence (signed-rank test, p = 0.002**).

D. Maps of T-maze showing the spatial distribution of z-scored values of CA1 beta power (left. max 1.49; min -0.19), PFC beta power (middle-left, max 1.63; min -0.18), CA1-PFC beta coherence (middle-right, max 1.16; min -0.19), and SWR rate (right, max 1.34; min 0). Plots are for a single session from one animal.

E. Number of SWR events per trial during odor sampling and reward consumption on correct trials across all animals (rank-sum test, n = 3157 trials, $p < 0.001$***). Error bars indicate s.e.m.

F. Beta (top row) and respiratory rhythm (RR) (bottom row) power on correct and incorrect trials in CA1, PFC, and OB. Error bars indicate 95% confidence intervals based on bootstrapped data. (Correct trials (n = 3174) were randomly subsampled with replacement to match the number of incorrect trials (n = 1008) 1000 times; beta power: CA1: $p = 0.016$*; PFC: $p < 0.001$***; OB: $p = 0.005$**. RR power: CA1: $p = 0.47$; PFC: $p = 0.06$; OB: $p = 0.43$).

G. Beta (top) and RR (bottom) CA1-PFC coherence on correct and incorrect trials. Error bars indicate 95% confidence intervals based on bootstrapped data. (beta coherence: $p = 0.005$**; RR coherence: $p = 0.41$).

H. Beta (top row) and RR (bottom row) CA1-PFC coherence as a function of decision latency after initial nosepoke on each correct trial. Decision latencies were divided into six equally sized subgroups (sextiles) for visualization, but correlation coefficients were calculated using all trials together. (n = 3174 trials, Beta: $r = -0.11$, $p = 1.7e-9$***; RR: $r = -0.013$, $p = 0.47$). Error bars indicate s.e.m.

Figure 3: Single neurons in CA1 and PFC exhibit choice-selectivity during odor sampling

A. Sankey diagram showing the number of CA1 cells that were classified into different categories. Sizes of partitions are proportional to raw numbers.

B. Example PSTH and raster plot for a single choice-selective CA1 neuron during odor sampling for correct trials, illustrating differential response to the two odors. Shaded areas indicate s.e.m.

C. PSTH and raster plot for the same neuron in (B), but only for incorrect trials.

D Selectivity index (SI) of all odor-selective cells in CA1 on correct trials (left) and incorrect trials (right), aligned to odor onset. SI is calculated as the difference in firing rate between Odor 1 trials and Odor 2 trials, divided by the sum of these firing rates. SI is color coded, where blue indicates an SI of 1 (absolute Odor 1 preference), red indicates an SI of -1 (absolute Odor 2 preference) and black indicates an SI of 0 (not selective). Cells are sorted according to peak selectivity on correct trials and sorting order is the same for both plots.

E. Correlation between correct trial SI and incorrect trial SI for all odor-selective CA1 cells ($r = -0.57$, $p = 7.6e-5$***).

F-J. Same as A-E, but for PFC cells. Correlation in J ($r = -0.71$, $p = 1.1e-8$***).

Figure 4: Neural ensemble responses emerge gradually during recall governed by beta coordination and predict the upcoming choice

A. Normalized firing rate of all odor-responsive cells in CA1 (top) and PFC (bottom) during a 1 second window after odor sampling.

B. Dissimilarity between population vectors (PVs) on Odor 1 versus Odor 2 presentations during the odor sampling period, for CA1 odor-responsive population (top, n = 125 cells)

and PFC odor-responsive population (bottom, n = 157 cells). Dissimilarity between PVs are scaled and shown as a PV differential index (PDI), where 0 indicates identical responses. Colored line indicates real data, grey shaded area indicates 95% confidence intervals of shuffled distribution.

C. PV divergence time in CA1 and PFC. Divergence time is quantified as the first time point where the real data PDI surpasses the mean + 2 s.d. of the shuffled PDI distribution (n = 50 samples with replacement, 500 iterations. Bootstrap test, p = 0.006**).

D. Timing of significant PV divergence in CA1 (top) and PFC (bottom) odor-responsive ensembles on each trial, represented by black dots. Shaded area represents the duration of time the rate spent in the nosepoke before executing a decision on each trial. Trials are sorted according to decision time latency.

E. PV divergence latency as a function of decision latency for CA1 (top) and PFC (bottom). PV divergence latencies were divided into six equally sized subgroups (sextiles) for visualization, but correlation coefficients were calculated using all trials together (CA1: r = 0.23, p = 2.5e-8***; PFC: r = 0.12, p =3.5e-4***).

F. PV divergence time as a function of beta coherence. PV divergence latencies were divided into six equally sized subgroups (sextiles) for visualization, but correlation coefficients were calculated using all trials together (CA1: r = -0.19, p = 1.4e-6***; PFC: r = 0.05, p = 0.13).

G. PV divergence time as a function of RR coherence sextiles (CA1: r = 0.008, p = 0.85; PFC: r = -0.009, p = 0.78).

H. Prediction of animal's choice of reward well by a GLM according to population spiking during odor sampling across varying length time windows. Colored error bars indicate real data mean +/- s.e.m, whereas grey error bars indicate shuffled data mean +/- s.e.m. Cells used for prediction include all odor-responsive cells in CA1 (left) and PFC (right). Stars indicate prediction time windows where the fraction of correctly predicted trials was significantly higher than the fraction from the shuffled data (rank-sum tests, * = p < 0.05).

Figure 5: Odor association representations and spatial representations on the track

A. Example association-selective units (CA1, first two columns, PFC, last two columns) with spatial fields on the track. Top row: Heat map of spatial fields during run bouts. Middle row: Linearized spatial tuning curves for outbound left and right run trajectories. Bottom row: PSTHs showing odor responses during memory-recall period (Odor selectivity indices, left to right: 0.92, -0.43, -0.40, -0.57).
B. Place field prevalence in odor unresponsive, and odor responsive cells in CA1 (left) and PFC (right). A total of 585 CA1 and 288 PFC task-active units were analyzed. (Binomial tests against non-responsive proportion, * = $p < 0.05$, ** = $p < 0.01$).
C. Correlation between firing rates during run and firing rates during odor sampling period for pyramidal cells in CA1 (left) and PFC (right). (Spearman rank-correlation, CA1: $r = 0.39$, $p = 3.0e-37$; PFC: $r = 0.68$, $p = 1.2e-62$)
D. Place field width for odor unresponsive and odor responsive units in CA1 (left) and PFC (right). If a unit had a firing field on both outbound trajectories, each field was counted separately. Rank-sum tests; CA1: n = 452 fields, $p = 0.15$; PFC: n = 207 fields, $p = 0.92$).
E. Association selectivity scores for trajectory-selective units and non-trajectory selective units (rank sum tests, CA1, left: $p = 0.74$; PFC, right: $p = 0.54$).
F. Trajectory selectivity scores of association selective units according to preferred odor association. (Rank sum tests, CA1: $p = 0.26$; PFC: $p = 0.20$).
G. Decoding of choice identity by naïve Bayesian Classifier according to CA1 (left) and PFC (right) odor-responsive ensemble activity at five equally sized spatial quintiles along the full run trajectory of the maze. 1 spatial quintile = 24.6 cm (123 cm / 5). Colored error bars indicate real data mean +/- s.e.m, whereas grey error bars indicate shuffled data

mean +/- s.e.m. Stars indicate quintiles where the fraction of correctly predicted trials was significantly higher than the fraction from the shuffled data (rank-sum test, * = $p < 0.05$).

H. Prediction of animal's choice of reward well by naive Bayesian Classifier according to CA1 (left) and PFC (right) spatially-modulated ensemble activity at five equally sized spatial quintiles encompassing the full maze. Colored error bars indicate real data mean +/- s.e.m, whereas grey error bars indicate shuffled data mean +/- s.e.m. Stars indicate quintiles where the fraction of correctly predicted trials was significantly higher than the fraction from the shuffled data (rank-sum test, * = $p < 0.05$, ** = $p < 0.01$).

Figure 6: CA1 and PFC cells phase lock to beta and respiratory rhythms during recall

All phase axes on spike-phase histograms are duplicated for visibility.

A. Example spike-phase histograms from two example cells that are phase locked to the beta rhythm. Top: CA1 cell (Rayleigh Z test, $z = 4.43$, $p = 0.011$); bottom: PFC cell ($z = 3.12$, $p = 0.04$).

B. Preferred beta phases of all odor-responsive cells. Top: CA1 cells ($n = 125$ cells, Rayleigh Z test, $z = 7.88$, $p = 3.4e-4$); bottom: PFC cells ($n = 157$ cells, $z = 0.91$, $p = 0.09$).

C. Polar histogram of preferred beta phases for all odor-responsive CA1 and PFC cells. Arrows indicate mean phase direction and magnitude.

D. Example spike-phase histograms from two example cells that are phase locked to RR. Top: CA1 cell (Rayleigh Z test, $z = 135.3$, $p = 6.3e-62$); bottom: PFC cell ($z = 73.9$, $p = 3.9e-37$).

E. Preferred RR phases of all odor-responsive cells. Top: CA1 cells (Rayleigh Z test, $z = 8.83$, $p < 0.001$) bottom: PFC cells ($z = 1.39$, $p = 0.24$).

F. Polar histogram of preferred RR phases for all odor-responsive CA1 and PFC cells. Arrows indicate mean phase direction and magnitude.

G. Rayleigh Z scores of spike-phases for all cells phase-locked to local beta rhythm on correct versus incorrect trials. (signed-rank tests, CA1: n = 17 cells, p = 0.002**; PFC: n = 7 cells, p = 0.38).

H. As in G, but for spike-phases for all cells phase-locked to local RR. (signed-rank tests, CA1: n = 80 cells, p = 0.36; PFC: n = 21 cells, p = 0.24).

I. Percentage of cells in CA1 and PFC that were phase locked to either beta or RR (z-tests for proportions; CA1: n = 36 cells phase-locked to beta, n = 112 cell phase-locked to RR, z = -9.8, p = 6.8e-23; PFC: n = 17 cells phase-locked to beta, n = 60 cells phase-locked to RR, z = -5.6, p = 8.8e-9).

J. Rayleigh Z scores for spike-phases of odor-responsive cells for beta and RR (rank-sum test; CA1: n = 125 cells, p = 1.5e-26***; PFC: n = 157 cells, p = 0.17).

K. Percentage of cells that are association-selective (solid bars), phase-locked to the beta rhythm (outlined bars), and both association-selective and phase-locked (striped bars). Grey bars indicate chance level of cells being both association-selective and phase-locked, error bars indicate the range of cell percentages that fall within the 95% bounds of the chance binomial distribution. (binomial test, CA1: p = 0.083; PFC: p = 0.16).

L. Percentage of cells that are association-selective (solid bars), phase-locked to RR (outlined bars), and both association-selective and phase-locked (striped bars). Grey bars indicate chance level of cells being both association-selective and phase-locked, error

bars indicate the range of cell percentages that fall within the 95% bounds of the chance binomial distribution. (Binomial test, CA1: $p = 0.077$; PFC: $p = 0.10$).

STAR★METHODS

LEAD CONTACT AND MATERIALS AVAILABILITY

Further information and requests for resources and reagents should be directed to the Lead Contact, Shantanu P. Jadhav (shantanu@brandeis.edu). This study did not generate new unique reagents.

EXPERIMENTAL MODEL AND SUBJECT DETAILS

All experimental procedures were approved by the Brandeis University Institutional Animal Care and Usage Committee (IACUC) and conformed to US National Institutes of Health guidelines. Eight male Long-Evans rats (3-6 months, 450-650 g) were used for experiments. Animals were housed individually in a dedicated climate-controlled animal facility on a 12-hour light/dark cycle. Upon arrival, animals were provided ad libitum access to food and water and handled regularly to habituate them to human contact.

METHODS DETAILS

Behavior Apparatus

An olfactometer (MedAssociates Inc.) was used for dispensing odors. The olfactometer continuously dispensed clean air to the nosepoke until receiving a signal to open a solenoid valve which caused air to flow through liquid odorants, resulting in odorized air dispensed to the nosepoke. A vacuum tube attached to the nosepoke was used to continuously collect any residual odorized air between trials. Infrared beams were used at the nosepoke and reward wells to determine the precise timing of entry and exit from these areas.

Odor-Place Association Task

Once rats reached a minimum threshold weight of 450 g, they were food restricted to no less than 85% of their free-feeding baseline weight. For initial behavioral training, rats were familiarized with the behavior room, the sleep box, running on a raised track to receive evaporated milk reward, and sniffing odors presented in the nosepoke port. Following this habituation, rats were trained to hold their nose in the nosepoke port for a minimum of 500 ms, with an auditory tone indicating when this 500-ms time threshold was reached, though rats could continue to sniff the odor for any longer duration of time. Throughout all training and experiments, if the rat exited the nosepoke before this threshold was reached, no reward was dispensed regardless of the rat's choice and the rat was required to re-initiate the trial. These prematurely terminated trials were excluded from all analyses.

Animals were subsequently trained on the olfactory association. On each trial, one of two possible odors was dispensed at the nosepoke in a pseudo-random order. Odor 1 (Heptanol – pine/citrus scent) indicated that the rat should go to Reward 1 to receive reward. Odor 2 (ethyl butyrate – strawberry scent) indicated that the rat should choose Reward 2 (**Figure 1A**). If the rat ultimately made the correct choice, evaporated milk reward would be dispensed at the chosen reward port, whereas upon an incorrect choice no reward was dispensed. Associative training was shaped in steps, with initial training on a shortened version of the maze with reward wells close to the nosepoke, and subsequent training on the full T-maze (81 cm long center stem, and 43cm long reward arms). Two rats performed the odor-association task without running the T-maze, and instead were just required to perform the association with the reward wells within easy reach on either side of the nosepoke. For one animal, the maze had a shortened stem (40 cm instead of 81 cm), but the reward wells were still at the ends of the T arms. Task performance

was calculated as the proportion of correct trials. Rats were trained until they could perform the task with at least 80% accuracy for 3 consecutive days.

Once training was complete, animals were once again provided with *ad libitum* access to food until they reached at least 600 g, before undergoing surgery. After surgery but before recording, rats were briefly re-trained on the association until they could again perform the task with at least 80% accuracy. On recording days, animals were allowed to continue performing the task until they reached satiation, about 100-150 trials per day. Task epochs were interleaved by sleep epochs, in which rats spent about 20 minutes in an opaque sleep box, with a sleep epoch as the first and last epoch of each day.

Surgical Procedures

Surgical implantation techniques were performed as described previously (Shin et al., 2019; Tang and Jadhav, 2019; Tang et al., 2017). Animals were implanted with a microdrive array containing 30 independently moveable tetrodes targeting right dorsal hippocampal region CA1 (-3.6 mm AP and +2.2 mm ML, 10-12 tetrodes), right PFC (+3.0 mm AP and +0.7 mm ML10-13 tetrodes), and right olfactory bulb (+7.2 mm AP and +0.8 mm ML, 1-4 tetrodes). Post-operative analgesic care was provided for 48 hours after surgery to minimize pain and discomfort. In two of the eight animals used for experiments, a nasal thermocouple was implanted in addition to the microdrive array to record the respiratory rhythm. The thermocouple was placed in the left nostril though a hole drilled in the skull at +7.5 mm anterior to the cribriform suture. The thermocouple wire was secured using dental acrylic and soldered to the same printed circuit board as the tetrodes.

Tetrode Recordings

For 1-2 weeks following surgery, tetrodes were gradually lowered to the desired depths. Hippocampal tetrodes were targeted to the pyramidal layer of CA1 using characteristic EEG patterns (sharp wave polarity, theta modulation) and neural firing patterns as previously described (Jadhav et al., 2012; Jadhav et al., 2016). The final placement of tetrodes was confirmed in histological preparations using Nissl staining post-mortem. One tetrode in corpus callosum served as hippocampal reference, and another tetrode in overlying cortical regions with no spiking signal served as PFC reference. A ground screw (GND) installed in the skull overlying cerebellum also served as a reference. All spiking activity was recorded relative to the local reference tetrode. Only LFP activity was recorded from olfactory bulb. Electrodes were not moved at least 4 hours before and during the recording day.

Data were collected using a SpikeGadgets data acquisition system (SpikeGadgets LLC) (Shin et al., 2019; Tang et al., 2017). Spike data were sampled at 30 kHz and bandpass filtered between 600 Hz and 6 kHz. LFP signals were sampled at 1.5 kHz and bandpass filtered between 0.5 Hz and 400 Hz. The animal's position and running speed were recorded with an overhead color CCD camera (30 fps) and tracked by color LEDs affixed to the headstage.

QUANTIFICATION AND STATISTICAL ANALYSIS

All data analysis was performed in MATLAB using custom code unless otherwise noted. Error bars indicate standard error of the mean (s.e.m.) unless otherwise noted. Significance was defined using an alpha of 0.05 unless otherwise noted. Statistical details including tests used, p-values, and n values can be found in figure legends, and are described in-depth below.

Local Field Potential

Trial-averaged spectrograms and coherograms were calculated using multi-taper spectral methods included in the Chronux package for MATLAB (www.chronux.org). To get the beta filtered local field potential (LFP) signal, raw LFP (with respect to GND) was band pass filtered at 15-30 Hz using a zero-phase IIR filter. Amplitude, phase and envelope magnitude of the signals were obtained using a Hilbert transform. Beta power and coherence were z-scored to the epoch mean.

Similarly, the respiratory rhythm signal was obtained by band pass filtering the raw LFP at 7-8 Hz. Due to the overlap between the RR and the theta rhythm (6-12 Hz), to get an accurate measure of RR power and coherence without leakage from the theta rhythm, this signal was z-scored to time-matched periods during immobility while the animal was consuming reward.

Sharp-Wave Ripple detection

Hippocampal sharp-wave ripples were detected as previously described (Jadhav et al., 2016; Shin et al., 2019; Tang et al., 2017). Briefly, the raw LFP signal from CA1 tetrodes was filtered in the ripple band (150-250 Hz), and the envelope of the ripple-filtered LFPs was determined using a Hilbert transform. SWR events were detected as contiguous periods when the envelope stayed above 3 SD of the mean on at least one tetrode for at least 15 ms.

Cross-frequency coupling

Phase-amplitude coupling between RR and beta was computed as described in (Tort et al., 2010). In brief, the phases of RR were binned, and the mean amplitude of the beta rhythm at each phase was calculated. The mean amplitudes were then normalized by dividing each bin by the sum of amplitudes across all bins. The strength of phase-amplitude coupling was determined by comparing the amplitude distribution to a uniform distribution by calculating the

modulation index (MI), which is based on the Kullback–Leibler (KL) distance but normalized so that values fall between 0 and 1, where a value of 0 indicates a uniform distribution of beta amplitudes across RR phases. Significance was determined by comparing the calculated MI to a null distribution generated by shuffling the trial number assignments of the RR phase series; this maintains the structure of the underlying rhythm but randomly aligns the beta amplitudes on each trial to each trial sequence RR phases.

Single Unit analysis

Spike sorting was done semi-automatically using MountainSort (Barnett et al., 2016; Chung et al., 2017), with manual curation. Only well-isolated units were used for analysis. Interneurons and pyramidal cells were classified based on average firing rate, with a cutoff of 9.5 Hz. Units were excluded from analysis if they had fewer than 100 spikes across all sessions. Pyramidal cells that only spiked during sleep epochs were excluded from analysis.

Odor Responsiveness

Odor responsiveness was calculated as a change in firing rate following odor sampling onset. For each trial, the odor sampling period was defined as the time from the onset when rat's nose broke the infrared beam to offset when the beam break was terminated. The pre-stimulus period was taken as that same duration leading up to the poke onset. Sampling events were only considered if the animal held it's nose in the odor port for longer than 0.50 seconds and proceeded to the correct reward port. Statistical significance was determined from the Wilcoxon signed rank test of those trial-matched rate differences for each odor identity separately. If a cell showed a significant change up or down from baseline for at least one of the odors, it was considered odor responsive. Of note, there was only a single unit analyzed whose

firing rate changed in opposite directions from baseline for the two odors, the remainder showed the same direction of change in firing rate for the two odors.

Odor Selectivity

Firing rates during odor sampling were calculated as the number of spikes as a function of time from the nosepoke onset to nosepoke offset. Odor selectivity was calculated using the following equation:

$$SI = \frac{\lambda_1 - \lambda_2}{\lambda_1 + \lambda_2}$$

Where λ_1 is the firing rate vector for Odor 1 trials, and λ_2 is firing rate vector for Odor 2 trials. *SI* = 1 indicates that the cell only responded on Odor 1 trials, whereas *SI* = -1 indicates that the cell only responded on Odor 2 trials. To determine significance, a null distribution was generated in which the odor identities were shuffled across trials. Cells were considered odor-selective if the SI fell outside of 1.5 s.d. from the mean of the null distribution.

Population Differential Index

The population differential index (PDI) was calculated as described in (Igarashi et al., 2014). For this analysis, all odor-responsive cells were pooled across animals and days into a single population. Mean firing rates were calculated in 100 ms bins from 0 to 1 second aligned to odor onset to obtain population vectors for each of the two odors. At each time bin, the correlation coefficient (CC) was calculated between the Odor 1 response vector and Odor 2 response vector. This CC was subtracted from 1 to obtain the PDI:

$$1 - CC = PDI$$

such that PDI = 1 indicates that the population responses for the two odors are completely distinct, whereas PDI = 0 indicates that the responses are identical. Chance-level PDI was computed by shuffling the odor identities across trials and creating a null distribution. The real PDI was then compared to the null distribution across the odor sampling time window. The timepoint at which the population responses to the odors were considered significantly distinct from each other was defined as the first timepoint at which the real PDI surpassed the 95% confidence interval of the null distribution.

Individual Trial PDI

A similar PDI analysis was employed to examine population dynamics on a trial-by-trial basis, in which the PDI was computed for single trials individually. Cells were not pooled across animals, and only sessions with at least 5 odor-responsive cells were considered for analysis. The PDI was computed by calculating the CC between the trial PV and the average PV of all trials of the opposite odor in that session. The timepoint of divergence of these two PVs was taken as the time at which this trial PDI surpassed the 95% CI of the null distribution from the full population analysis.

GLM

A generalized liner model (GLM) with a log link function was constructed to predict reward choice based on neural activity during the odor sampling period. Activity from all odor-responsive neurons that were active on at least 10 trials was included. Neural population activity from different length time bins from 0.1 seconds to 1 second aligned to odor onset was used for

prediction, i.e. 0-0.1s, 0-0.2s … 0-1.0s. Five-fold cross validation was used to test prediction. For each fold, the session's trials were randomly partitioned into five equally sized sets. Four of the five sets were used to train the GLM model and the remaining set was used to test. The prediction accuracy was calculated by dividing the number of correctly predicted trials by the total number of trials used for testing for each fold.

Significance was determined by performing the same procedure as described above but shuffling the trial outcomes to obtain a null distribution. At each time bin used for the prediction, a rank-sum test was performed on the prediction accuracy using the real data compared to the shuffled data.

Bayesian Decoder

Choice Identity decoding was performed as previously described (Karlsson & Frank, 2009). Briefly, a memoryless Bayesian decoder was built for each of the two choice identities from spikes occurring in the odor sampling period. Then, the likelihood of each choice (x) was reconstructed from their posterior probabilities given the spikes occurring at each segment along the maze on each run (p(x | spikes) = p(spikes | x) * p(x) / p(spikes)). Run activity was defined as contiguous bouts following the odor sampling period when the animal was traveling above 3 cm/sec, and to prevent overlap between odor spiking and run spiking, runs commenced ½ second after odor sampling ended, as determined by nosepoke offset. We assumed that the N active cells fired independently and followed a Poisson process, giving the following equation.

$$P(X|spikes) = C * (\prod_{i=1}^{N} f_i(X)^{spikes_i}) * e^{-\tau} \sum_{i=1}^{N} f(X)$$

Where C is a normalization constant across the two choice identities. The p-value was calculated from the Gaussian statistics of a Monte Carlo random shuffle (200 shuffles) of choice

identity during the odor sampling period. When choice identity decoding was calculated from the likelihoods of activity from each run, the decoding was performed in the same 5-fold leave-one-out fashion as was used in the GLM analyses, and the p value was calculated from the same Monte Carlo random shuffle of the training set route identities as the odor period based decoding.

Phase Locking

For all phase-locking analyses, the tetrode in each region with the most cells on each given day was used to measure oscillatory phase of either beta or RR. Phase locking of individual cells to the beta and respiratory rhythms was calculated by pooling the spike phases of each cell during the odor-sampling periods and performing a Rayleigh Z test for circular non-uniformity. For each cell, the mean direction of the von Mises distribution of spike-phases was used as the preferred phase. To compare phase-locking on correct and incorrect trials, correct trials were randomly subsampled with replacement to match the number of incorrect trials 1000 times. A Rayleigh Z score was calculated based on spike phases from each these subsampled datasets. The mean Rayleigh Z score for each cell from the bootstrapped distribution was then compared to the Rayleigh Z score on incorrect trials.

Occupancy maps

For all place field analyses, only the 5 animals that were trained on the full T-maze were used; the three animals trained on the truncated maze were excluded. Two-dimensional occupancy maps were by calculating occupancy in 2-cm square spatial bins from epochs in

which the animals running speed exceeded 3 cm/sec and convolving with a 2d Gaussian (σ= 2 pixels).

Place field determination

2-D Occupancy-normalized firing rate maps were then generated by dividing the spikes at each 2-D pixel by the unsmoothed occupancy at that pixel, and then and smoothing with a Gaussian kernel of (σ=2 pixels, or 4 cm).

Linearized trajectory occupancy maps were calculated as previously described (Jadhav et al., 2012; Shin et al., 2019; Tang et al., 2017). Briefly, the rats 2d spatial coordinates were first segmented into run epochs based on contiguous bouts of time in which the animals running speed exceeded 3 cm/sec. Then, the position of the animal during each 'run epoch' was categorized by its origin and destination, and each position was assigned to one of 100 (1.23 cm) bins from the origin to the destination of that route. Then the total number of spikes at each bin was divided by that bin's occupancy, and the map was convolved by a Gaussian kernel with a standard deviation of 2 pixels (2.5 cm).

Place field peak was calculated as the peak rate bin on the smoothened, linearized rate map, and place fields were only considered for trajectories in which the cell had a peak firing rate of at least 1 Hz. Place field width was calculated using a flood fill-algorithm in which the edges were defined as the closest bins to the peak bin in which the rate fell below 25% of the peak rate. Place field sparsity and information scores were calculated as previously described (Skaggs et al., 1993). A cell was determined to have a place field if its peak firing rate along that trajectory was ≥ 2 S.D. above the mean of a bootstrapped distribution generated by circular shifting the spikes in time for each individual run, and the field covered less than 75% of the linearized trajectory. When analyzing the place field characteristics of odor selective cells

(Figure 5, Figure S5), the field of each outbound journey was analyzed separately so as to prevent ‘choosing’ certain fields over others.

Trajectory selectivity

Trajectory selective cells were identified using a previously validated method (Shin et al., 2019). Briefly, the linearized spatial tuning curve was calculated separately for each outbound trajectory and the correlation between those trajectories was computed. A cell was identified as trajectory selective if this correlation value exceeded the 95th percentile of a bootstrap distribution wherein each outbound trajectory identity was shuffled and the correlation recalculated.

To measure trajectory selectivity as it related to recall period selectivity we used an analogous method to the odor selectivity index. Briefly we calculated the mean firing rate along each run beginning one half second following nosepoke termination and once the animals speed exceeded 3 cm/sec to the end of that run (when the animal either reached the goal or its velocity fell below 3 cm/sec for more than ½ second). The difference in these mean firing rates across runs was divided by the sum of those two mean rates to generate a trajectory selectivity index.

REFERENCES

Abraham, N.M., Spors, H., Carleton, A., Margrie, T.W., Kuner, T., and Schaefer, A.T. (2004). Maintaining accuracy at the expense of speed: Stimulus similarity defines odor discrimination time in mice. Neuron 44, 865-876.

Allen, T.A., Salz, D.M., Mckenzie, S., and Fortin, N.J. (2016). Nonspatial Sequence Coding in CA1 Neurons. J Neurosci 36, 1547-1563.

Alvarez, P., Wendelken, L., and Eichenbaum, H. (2002). Hippocampal formation lesions impair performance in an odor-odor association task independently of spatial context. Neurobiol Learn Mem 78, 470-476.

Barnett, A.H., Magland, J.F., and Greengard, L.F. (2016). Validation of Neural Spike Sorting Algorithms Without Ground-Truth Information. J Neurosci Methods 264, 65-77.

Battaglia, F.P., Benchenane, K., Sirota, A., Pennartz, C.M., and Wiener, S.I. (2011). The hippocampus: hub of brain network communication for memory. Trends Cogn Sci 15, 310-318.

Benchenane, K., Peyrache, A., Khamassi, M., Tierney, P.L., Gioanni, Y., Battaglia, F.P., and Wiener, S.I. (2010). Coherent theta oscillations and reorganization of spike timing in the hippocampal-prefrontal network upon learning. Neuron 66, 921-936.

Benchenane, K., Tiesinga, P.H., and Battaglia, F.P. (2011). Oscillations in the prefrontal cortex: a gateway to memory and attention. Curr Opin Neurobiol 21, 475-485.

Beshel, J., Kopell, N., and Kay, L.M. (2007). Olfactory bulb gamma oscillations are enhanced with task demands. J Neurosci 27, 8358-8365.

Buschman, T.J., Denovellis, E.L., Diogo, C., Bullock, D., and Miller, E.K. (2012). Synchronous oscillatory neural ensembles for rules in the prefrontal cortex. Neuron 76, 838-846.

Buzsáki, G. (2015). Hippocampal sharp wave-ripple: A cognitive biomarker for episodic memory and planning. Hippocampus 25, 1073-1188.

Buzsaki, G., and Draguhn, A. (2004). Neuronal oscillations in cortical networks. Science 304, 1926-1929.

Buzsaki, G., Leung, L.W., and Vanderwolf, C.H. (1983). Cellular bases of hippocampal EEG in the behaving rat. Brain Res 287, 139-171.

Carr, M.F., Jadhav, S.P., and Frank, L.M. (2011). Hippocampal replay in the awake state: a potential substrate for memory consolidation and retrieval. Nat Neurosci 14, 147-153.

Cenquizca, L.A., and Swanson, L.W. (2007). Spatial organization of direct hippocampal field CA1 axonal projections to the rest of the cerebral cortex. Brain Res Rev 56, 1-26.

Chi, V.N., Müller, C., Se Wolfenstetter, T., Yanovsky, Y., Draguhn, A., Adriano, X., Tort, B.L., and Brankačk, J. (2016). Hippocampal Respiration-Driven Rhythm Distinct from Theta Oscillations in Awake Mice. J Neurosci 36, 162-177.

Chung, J.E., Magland, J.F., Barnett, A.H., Tolosa, V.M., Tooker, A.C., Lee, K.Y., Shah, K.G., Felix, S.H., Frank, L.M., and Greengard, L.F. (2017). A Fully Automated Approach to Spike Sorting. Neuron 95, 1381-1394.

Churchwell, J.C., Morris, A.M., Musso, N.D., and Kesner, R.P. (2010). Prefrontal and hippocampal contributions to encoding and retrieval of spatial memory. Neurobiol Learn Mem 93, 415-421.

Colgin, L.L. (2011). Oscillations and hippocampal-prefrontal synchrony. Curr Opin Neurobiol 21, 467-474.

Delatour, B., and Witter, M.P. (2002). Projections from the parahippocampal region to the prefrontal cortex in the rat: evidence of multiple pathways. Eur J Neurosci 15, 1400--1407.

DeNardo, L.A., Liu, C.D., Allen, W.E., Adams, E.L., Friedmann, D., Fu, L., Guenthner, C.J., Tessier-Lavigne, M., and Luo, L. (2019). Temporal evolution of cortical ensembles promoting remote memory retrieval. Nat Neurosci 22, 460-469.

Eichenbaum, H. (1998). Using olfaction to study memory. Ann N Y Acad Sci 855, 657-669.

Eichenbaum, H., Fagan, A., and Cohen, N.J. (1986). Normal olfactory discrimination learning set and facilitation of reversal learning after medial-temporal damage in rats: implications for an account of preserved learning abilities in amnesia. J Neurosci 6, 1876-1884.

Eichenbaum, H., Kuperstein, M., Fagan, A., and Nagode, J. (1987). Cue-sampling and goal-approach correlates of hippocampal unit activity in rats performing an odor-discrimination task. J Neurosci 7, 716-732.

Euston, D.R., Gruber, A.J., and McNaughton, B.L. (2012). The role of medial prefrontal cortex in memory and decision making. Neuron 76, 1057-1070.

Ferbinteanu, J., Shirvalkar, P., and Shapiro, M.L. (2011). Memory modulates journey-dependent coding in the rat hippocampus. J Neurosci 31, 9135-9146.

Fitzgerald, J.K., Freedman, D.J., and Assad, J.A. (2011). Generalized associative representations in parietal cortex. Nat Neurosci 14, 1075-1079.

Floresco, S.B., Seamans, J.K., and Phillips, A.G. (1997). Selective roles for hippocampal, prefrontal cortical, and ventral striatal circuits in radial-arm maze tasks with or without a delay. J Neurosci 17, 1880-1890.

Fortin, N.J., Wright, S.P., and Eichenbaum, H. (2004). Recollection-like memory retrieval in rats is dependent on the hippocampus. Nature 431, 188-191.

Frederick, D.E., Brown, A., Brim, E., Mehta, N., Vujovic, M., and Kay, L.M. (2016). Gamma and Beta Oscillations Define a Sequence of Neurocognitive Modes Present in Odor Processing. J Neurosci 36, 7750-7767.

Fujisawa, S., Amarasingham, A., Harrison, M.T., and Buzsaki, G. (2008). Behavior-dependent short-term assembly dynamics in the medial prefrontal cortex. Nat Neurosci 11, 823-833.

Fujisawa, S., and Buzsaki, G. (2011). A 4 Hz oscillation adaptively synchronizes prefrontal, VTA, and hippocampal activities. Neuron 72, 153-165.

Gordon, J.A. (2011). Oscillations and hippocampal-prefrontal synchrony. Curr Opin Neurobiol 21, 486-491.

Gothard, K.M., Skaggs, W.E., Moore, K.M., and McNaughton, B.L. (1996). Binding of hippocampal CA1 neural activity to multiple reference frames in a landmark-based navigation task. J Neurosci 16, 823-835.

Hasegawa, I. (2000). Neural mechanisms of memory retrieval: role of the prefrontal cortex. Rev Neurosci 11, 113-125.

Hyman, J.M., Ma, L., Balaguer-Ballester, E., Durstewitz, D., and Seamans, J.K. (2012). Contextual encoding by ensembles of medial prefrontal cortex neurons. Proc Natl Acad Sci U S A 109, 5086-5091.

Hyman, J.M., Zilli, E.A., Paley, A.M., and Hasselmo, M.E. (2010). Working Memory Performance Correlates with Prefrontal-Hippocampal Theta Interactions but not with Prefrontal Neuron Firing Rates. Front Integr Neurosci 4, 2.

Igarashi, K.M., Lu, L., Colgin, L.L., Moser, M.B., and Moser, E.I. (2014). Coordination of entorhinal-hippocampal ensemble activity during associative learning. Nature 510, 143-147.

Ito, H.T., Zhang, S.J., Witter, M.P., Moser, E.I., and Moser, M.B. (2015). A prefrontal-thalamo-hippocampal circuit for goal-directed spatial navigation. Nature 522, 50-55.

Jadhav, S.P., Kemere, C., German, P.W., and Frank, L.M. (2012). Awake hippocampal sharp-wave ripples support spatial memory. Science 336, 1454-1458.

Jadhav, S.P., Rothschild, G., Roumis, D.K., and Frank, L.M. (2016). Coordinated excitation and inhibition of prefrontal ensembles during awake hippocampal sharp-wave ripple events. Neuron 90, 113-127.

Jones, M.W., and Wilson, M.A. (2005). Theta rhythms coordinate hippocampal-prefrontal interactions in a spatial memory task. PLoSBiol 3, e402.

Joo, H.R., and Frank, L.M. (2018). The hippocampal sharp wave-ripple in memory retrieval for immediate use and consolidation. Nat Rev Neurosci 19, 744-757.

Kay, L.M. (2005). Theta oscillations and sensorimotor performance. Proc Natl Acad Sci USA 102, 3863-3868.

Kay, L.M., and Beshel, J. (2010). A beta oscillation network in the rat olfactory system during a 2-alternative choice odor discrimination task. J Neurophysiol 104, 829-839.

Kepecs, A., Uchida, N., and Mainen, Z.F. (2006). The Sniff as a Unit of Olfactory Processing. Chemical Senses 31, 167-179.

Komorowski, R.W., Manns, J.R., and Eichenbaum, H. (2009). Robust conjunctive item-place coding by hippocampal neurons parallels learning what happens where. J Neurosci 29, 9918-9929.

Lee, I., and Solivan, F. (2008). The roles of the medial prefrontal cortex and hippocampus in a spatial paired-association task. Learning & Memory 15, 357-367.

Liu, X., Ramirez, S., Pang, P.T., Puryear, C.B., Govindarajan, A., Deisseroth, K., and Tonegawa, S. (2012). Optogenetic stimulation of a hippocampal engram activates fear memory recall. Nature 484, 381-385.

Lockmann, A.L.V., Laplagne, D.A., Leão, R.N., and Tort, A.B.L. (2016). A Respiration-Coupled Rhythm in the Rat Hippocampus Independent of Theta and Slow Oscillations. J Neurosci 36, 5338-5352.

Maharjan, D.M., Dai, Y.Y., Glantz, E.H., and Jadhav, S.P. (2018). Disruption of dorsal hippocampal - prefrontal interactions using chemogenetic inactivation impairs spatial learning. Neurobiol Learn Mem 155, 351-360.

Martin, C., Beshel, J., and Kay, L.M. (2007). An olfacto-hippocampal network is dynamically involved in odor-discrimination learning. J Neurophysiol 98, 2196-2205.

McKenzie, S., Frank, A.J., Kinsky, N.R., Porter, B., Rivière, P.D., and Eichenbaum, H. (2014). Hippocampal representation of related and opposing memories develop within distinct, hierarchically organized neural schemas. Neuron 83, 202-215.

Miller, E.K., and Cohen, J.D. (2001). An integrative theory of prefrontal cortex function. Annu Rev Neurosci 24, 167-202.

Moita, M.A., Rosis, S., Zhou, Y., LeDoux, J.E., and Blair, H.T. (2003). Hippocampal place cells acquire location-specific responses to the conditioned stimulus during auditory fear conditioning. Neuron 37, 485-497.

Moser, M.B., and Moser, E.I. (1998). Distributed encoding and retrieval of spatial memory in the hippocampus. J Neurosci 18, 7535--7542.

Norman, Y., Yeagle, E.M., Khuvis, S., Harel, M., Mehta, A.D., and Malach, R. (2019). Hippocampal sharp-wave ripples linked to visual episodic recollection in humans. Science 365.

O'Neill, P.K., Gordon, J.A., and Sigurdsson, T. (2013). Theta oscillations in the medial prefrontal cortex are modulated by spatial working memory and synchronize with the hippocampus through its ventral subregion. J Neurosci 33, 14211-14224.

Otto, T., and Eichenbaum, H. (1992a). Complementary roles of the orbital prefrontal cortex and the perirhinal- entorhinal cortices in an odor-guided delayed-nonmatching-to-sample task. Behav Neurosci 106, 762-775.

Otto, T., and Eichenbaum, H. (1992b). Neuronal activity in the hippocampus during delayed non-match to sample performance in rats: evidence for hippocampal processing in recognition memory. Hippocampus 2, 323-334.

Papale, A.E., Zielinski, M.C., Frank, L.M., Jadhav, S.P., and Redish, A.D. (2016). Interplay between hippocampal sharp-wave-ripple events and vicarious trial and error behaviors in decision making. Neuron 92, 975-982.

Paxinos, G., and Watson, C. (2004). The Rat Brain in Stereotaxic Coordinates (Academic Press).

Peters, G.J., David, C.N., Marcus, M.D., and Smith, D.M. (2013). The medial prefrontal cortex is critical for memory retrieval and resolving interference. Learning & Memory 20, 201-209.

Place, R., Farovik, A., Brockmann, M., and Eichenbaum, H. (2016). Bidirectional prefrontal-hippocampal interactions support context-guided memory. Nat Neurosci.

Rangel, L.M., Rueckemann, J.W., Riviere, P.D., Keefe, K.R., Porter, B.S., Heimbuch, I.S., Budlong, C.H., and Eichenbaum, H. (2016). Rhythmic coordination of hippocampal neurons during associative memory processing. Elife 5.

Rinberg, D., Koulakov, A., and Gelperin, A. (2006). Speed-accuracy tradeoff in olfaction. Neuron 51, 351-358.

Schoenbaum, G., and Eichenbaum, H. (1995). Information coding in the rodent prefrontal cortex. II. Ensemble activity in orbitofrontal cortex. J Neurophysiol 74, 751-762.

Shin, J.D., and Jadhav, S.P. (2016). Multiple modes of hippocampal-prefrontal interactions in memory-guided behavior. Curr Opin Neurobiol 40, 161-169.

Shin, J.D., Tang, W., and Jadhav, S.P. (2019). Dynamics of Awake Hippocampal-Prefrontal Replay for Spatial Learning and Memory-Guided Decision Making. Neuron 104, 1110-1125.

Siegle, J.H., and Wilson, M.A. (2014). Enhancement of encoding and retrieval functions through theta phase-specific manipulation of hippocampus. Elife 3, e03061.

Skaggs, W.E., McNaughton, B.L., Gothard, K., and Markus, E. (1993). An information theoretic approach to deciphering the hippocampal code. In Advanced in Neural Information Processing Systems, S. Hanson, J.D. Cowan, and C.L. Giles, eds. (San Mateo, CA: Morgan Kaufmann Publishers), pp. 1030-1037.

Stopfer, M., Jayaraman, V., and Laurent, G. (2003). Intensity versus identity coding in an olfactory system. Neuron 39, 991-1004.

Tang, W., and Jadhav, S.P. (2019). Sharp-wave ripples as a signature of hippocampal-prefrontal reactivation for memory during sleep and waking states. Neurobiol Learn Mem 160, 11-20.

Tang, W., Shin, J.D., Frank, L.M., and Jadhav, S.P. (2017). Hippocampal-prefrontal reactivation during learning is stronger in awake compared with sleep states. J Neurosci 37, 11789-11805.

Terada, S., Sakurai, Y., Nakahara, H., and Fujisawa, S. (2017). Temporal and Rate Coding for Discrete Event Sequences in the Hippocampus. Neuron 94, 1248-1262.

Tort, A.B., Komorowski, R., Eichenbaum, H., and Kopell, N. (2010). Measuring phase-amplitude coupling between neuronal oscillations of different frequencies. J Neurophysiol 104, 1195-1210.

Tort, A.B., Komorowski, R.W., Manns, J.R., Kopell, N.J., and Eichenbaum, H. (2009). Theta-gamma coupling increases during the learning of item-context associations. Proc Natl Acad Sci U S A 106, 20942-20947.

Uchida, N., and Mainen, Z.F. (2003). Speed and accuracy of olfactory discrimination in the rat. Nat Neurosci 6, 1224-1229.

Verhagen, J.V., Wesson, D.W., Netoff, T.I., White, J.a., and Wachowiak, M. (2007). Sniffing controls an adaptive filter of sensory input to the olfactory bulb. Nature Neuroscience 10, 631-639.

Wiener, S.I., Paul, C.A., and Eichenbaum, H. (1989). Spatial and behavioral correlates of hippocampal neuronal activity. Journal of Neuroscience 9, 2737-2763.

Wikenheiser, A.M., and Redish, A.D. (2015). Hippocampal theta sequences reflect current goals. Nat Neurosci 18, 289-294.

Wiltgen, B.J., Brown, R.A., Talton, L.E., and Silva, A.J. (2004). New circuits for old memories: the role of the neocortex in consolidation. Neuron 44, 101-108.

Wiltgen, B.J., Zhou, M., Cai, Y., Balaji, J., Karlson, M.G., Parivash, S.N., Li, W., and Silva, A.J. (2010). The hippocampus plays a selective role in the retrieval of detailed context memories. Curr Biol 20, 1336-1344.

Wirth, S., Avsar, E., Chiu, C.C., Sharma, V., Smith, A.C., Brown, E., and Suzuki, W.A. (2009). Trial outcome and associative learning signals in the monkey hippocampus. Neuron 61, 930-940.

Wirth, S., Yanike, M., Frank, L.M., Smith, A.C., Brown, E.N., and Suzuki, W.A. (2003). Single neurons in the monkey hippocampus and learning of new associations. Science 300, 1578-1581.

Yanike, M., Wirth, S., and Suzuki, W.A. (2004). Representation of well-learned information in the monkey hippocampus. Neuron 42, 477-487.

Yu, J.Y., and Frank, L.M. (2015). Hippocampal-cortical interaction in decision making. Neurobiol Learn Mem 117, 34-41.

Zielinski, M.C., Shin, J.D., and Jadhav, S.P. (2019). Coherent Coding of Spatial Position Mediated by Theta Oscillations in the Hippocampus and Prefrontal Cortex. J Neurosci 39, 4550-4565.

Zielinski, M.C., Tang, W., and Jadhav, S.P. (2017). The role of replay and theta sequences in mediating hippocampal-prefrontal interactions for memory and cognition. Hippocampus.

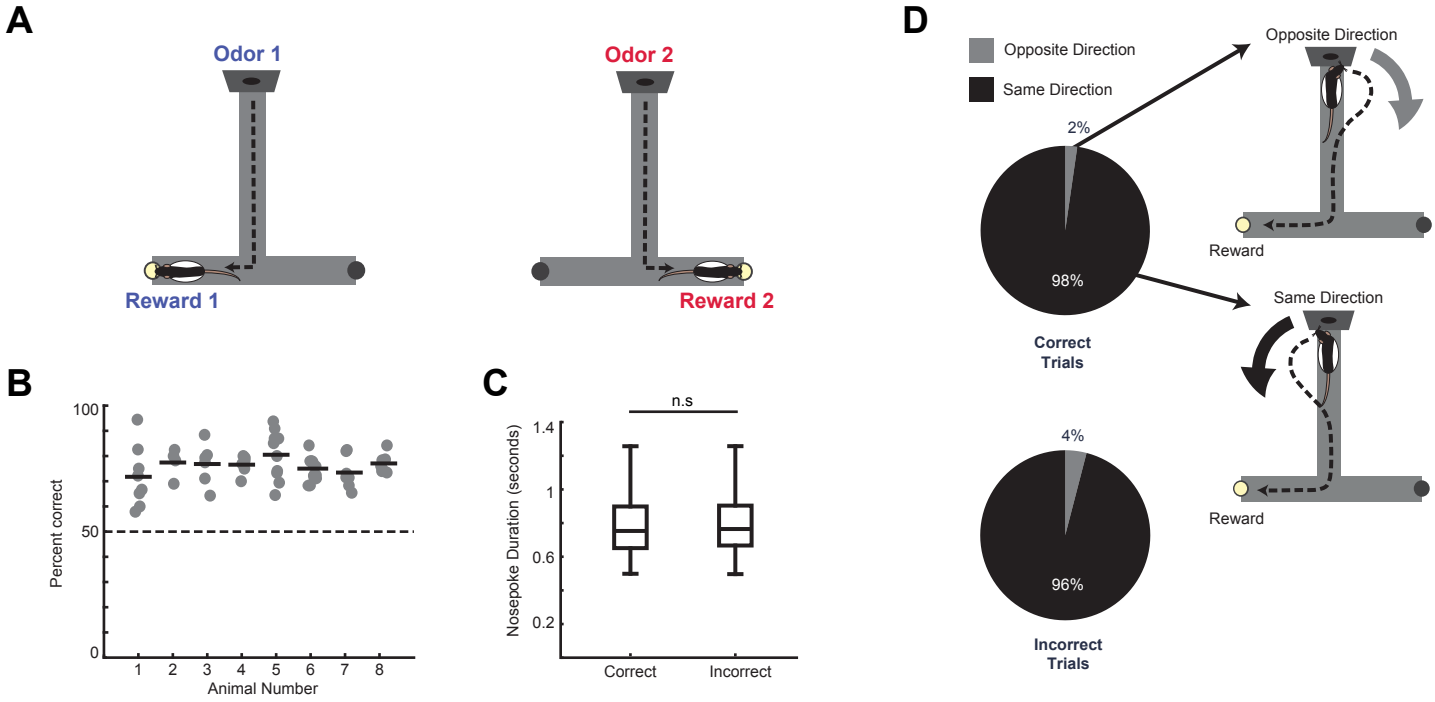
A
Odor 1
Reward 1
Odor 2
Reward 2
B
Percent correct
100
50
0
1 2 3 4 5 6 7 8
Animal Number
C
n.s
Nosepoke Duration (seconds)
1.4
1
0.6
0.2
Correct
Incorrect
D
Opposite Direction
Same Direction
2%
98%
Correct Trials
4%
96%
Incorrect Trials
Opposite Direction
Reward
Same Direction
Reward

Figure 1

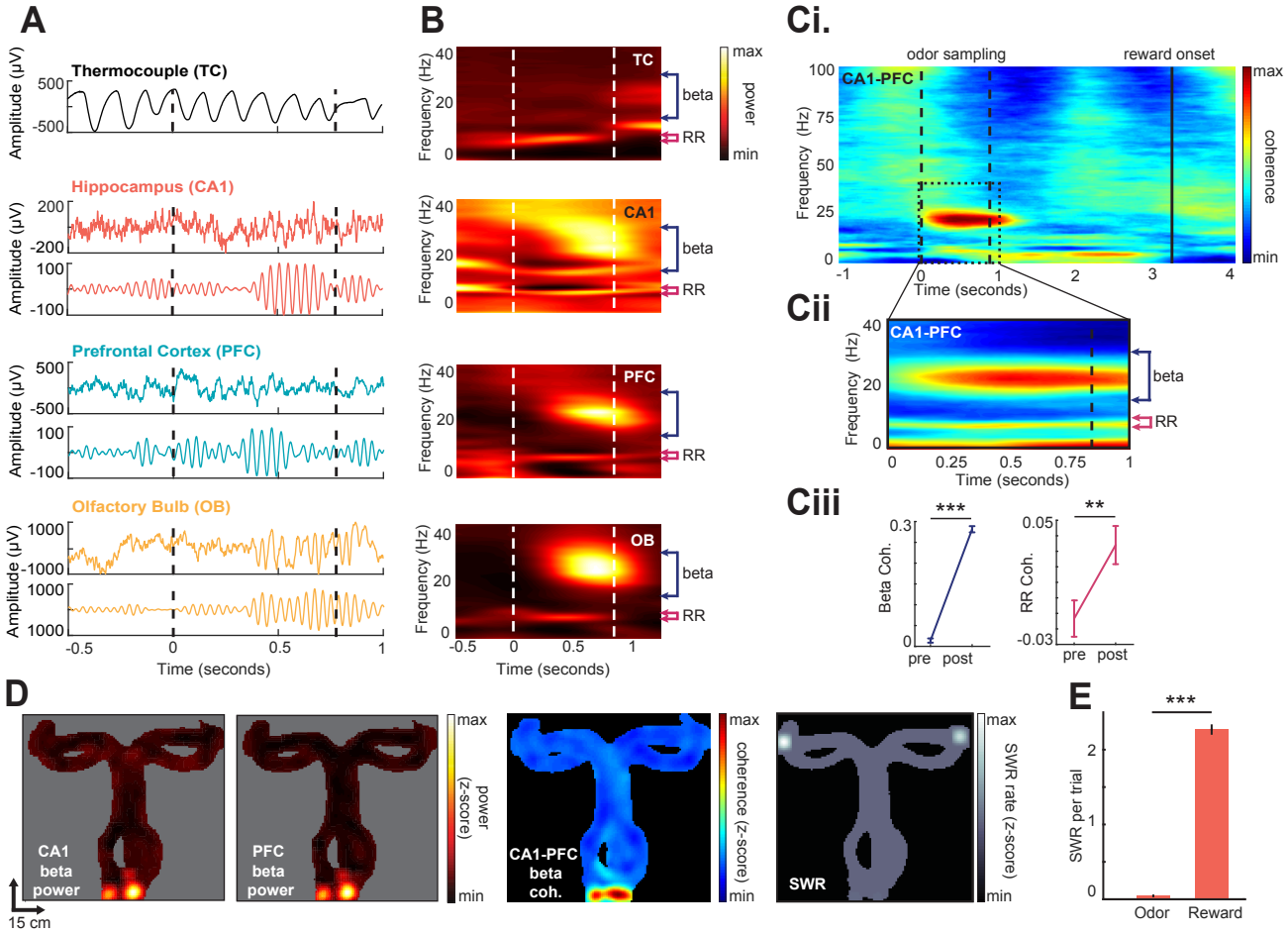
A
Thermocouple (TC)
Hippocampus (CA1)
Prefrontal Cortex (PFC)
Olfactory Bulb (OB)
Amplitude (μV)
Time (seconds)
B
TC
CA1
PFC
OB
Frequency (Hz)
beta
RR
max
power
min
Ci.
odor sampling
reward onset
CA1-PFC
Frequency (Hz)
Time (seconds)
coherence
Cii
Ciii
Beta Coh.
RR Coh.
pre
post

D
CA1 beta power
PFC beta power
CA1-PFC beta coh.
SWR
max
min
power (z-score)
coherence (z-score)
SWR rate (z-score)
15 cm
E
SWR per trial
Odor
Reward

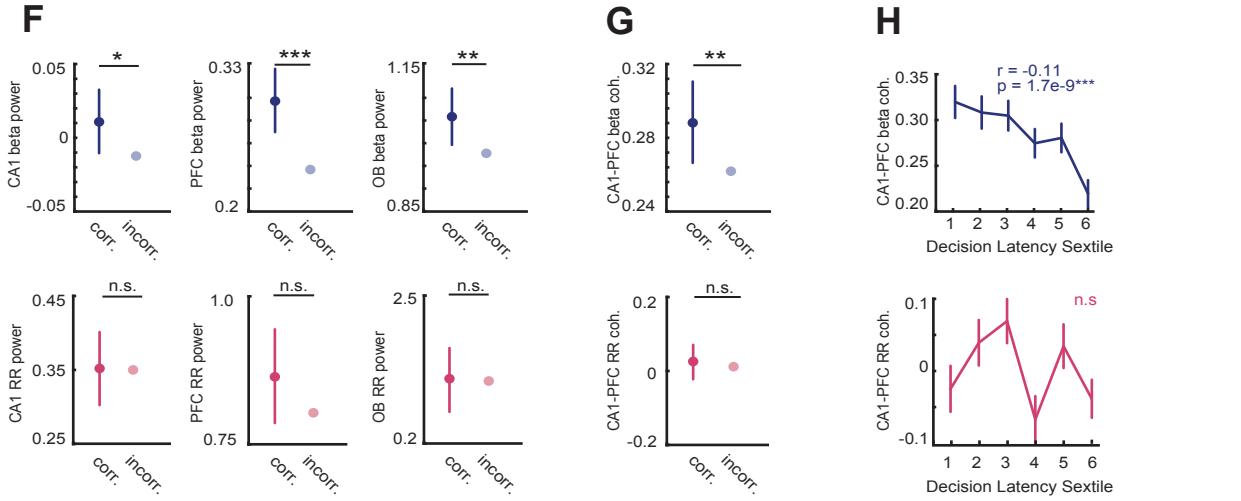
F
CA1 beta power
PFC beta power
OB beta power
CA1 RR power
PFC RR power
OB RR power
n.s.
corr.
incorr.
G
CA1-PFC beta coh.
CA1-PFC RR coh.
H
r = -0.11
p = 1.7e-9***
Decision Latency Sextile
n.s

Figure 2

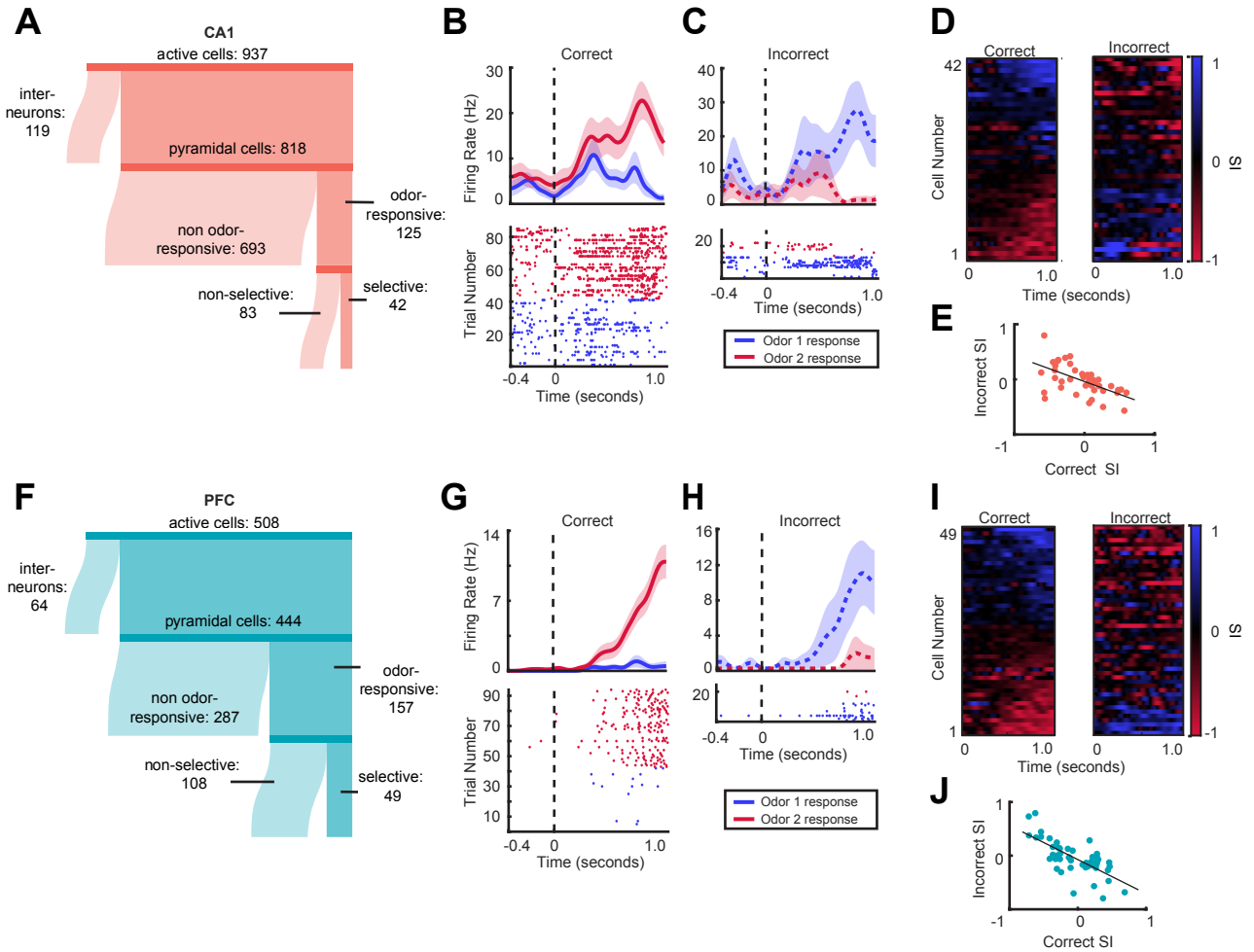
A
CA1
active cells: 937
inter-neurons: 119
pyramidal cells: 818
non odor-responsive: 693
odor-responsive: 125
non-selective: 83
selective: 42
B
Correct
Firing Rate (Hz)
Trial Number
Time (seconds)
C
Incorrect
Time (seconds)
Odor 1 response
Odor 2 response
D
Correct
Incorrect
Cell Number
Time (seconds)
SI
E
Incorrect SI
Correct SI
F
PFC
active cells: 508
inter-neurons: 64
pyramidal cells: 444
non odor-responsive: 287
odor-responsive: 157
non-selective: 108
selective: 49
G
Correct
Firing Rate (Hz)
Trial Number
Time (seconds)
H
Incorrect
Time (seconds)
Odor 1 response
Odor 2 response
I
Correct
Incorrect
Cell Number
Time (seconds)
SI
J
Incorrect SI
Correct SI

Figure 3

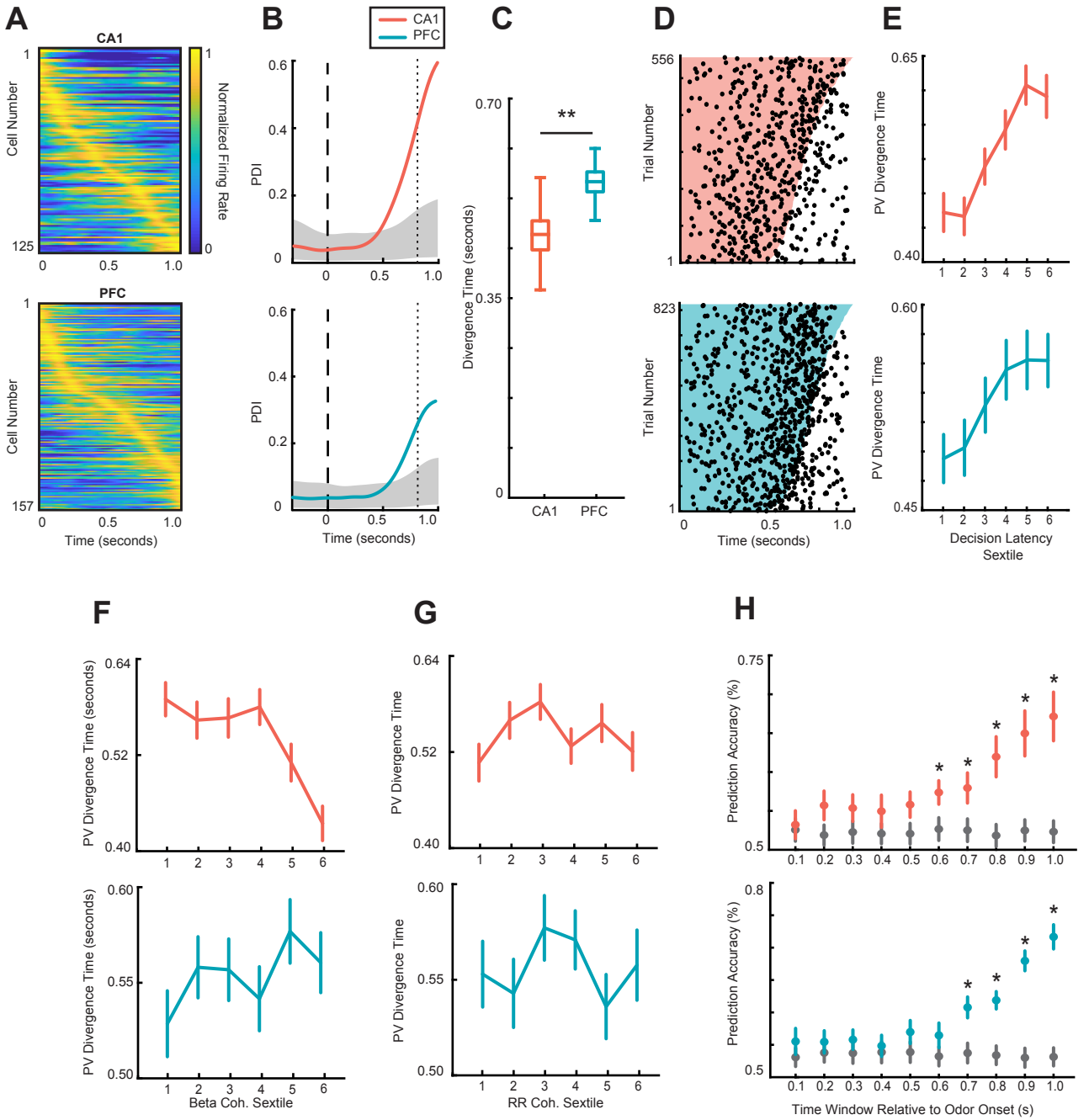
A
CA1
Cell Number
Normalized Firing Rate
PFC
Time (seconds)
B
CA1
PFC
PDI
Time (seconds)
C
Divergence Time (seconds)
**
CA1
PFC
D
Trial Number
Time (seconds)
E
PV Divergence Time
Decision Latency Sextile
F
PV Divergence Time (seconds)
Beta Coh. Sextile
G
PV Divergence Time
RR Coh. Sextile
H
Prediction Accuracy (%)
Time Window Relative to Odor Onset (s)

Figure 4

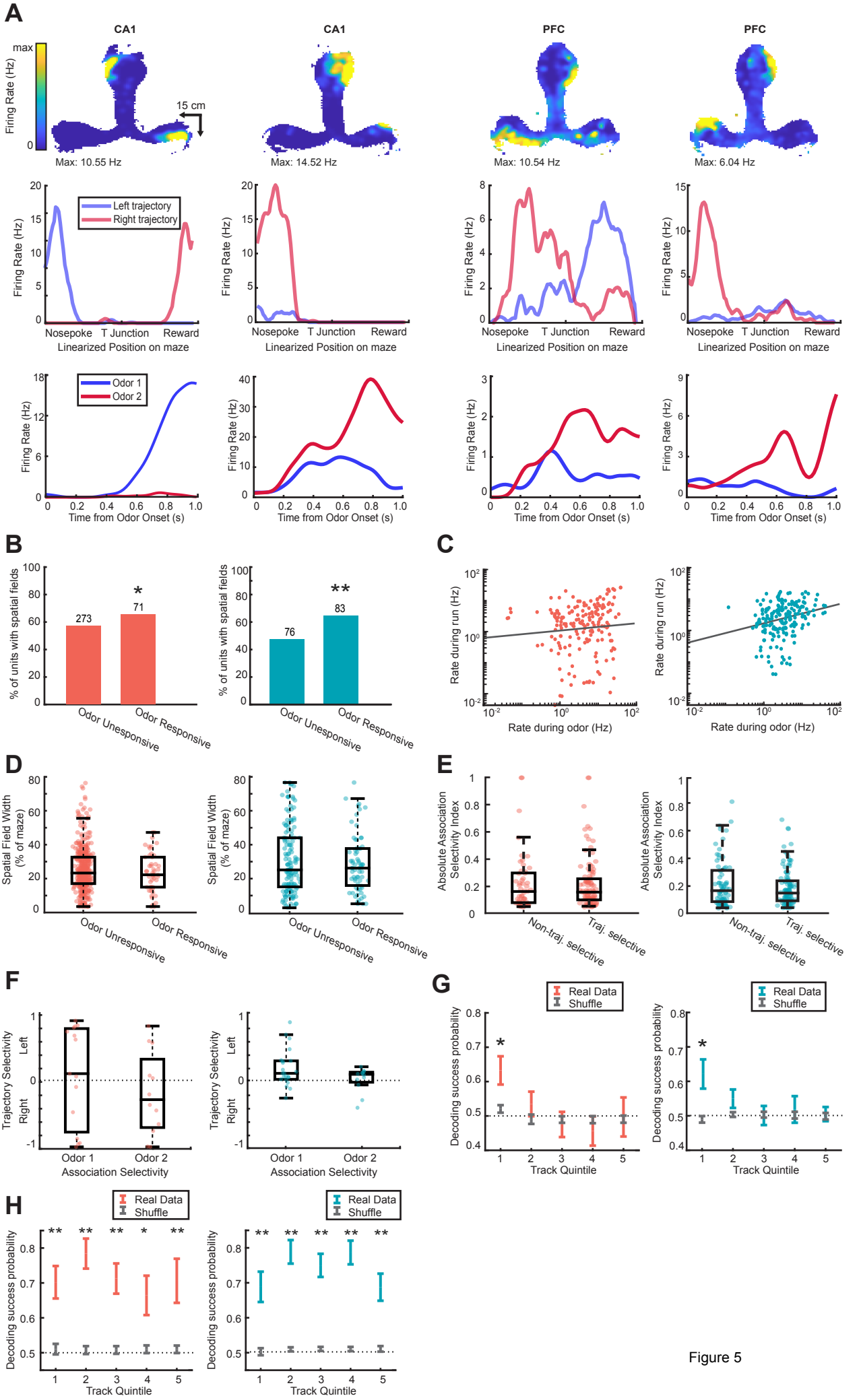
A
CA1
CA1
PFC
PFC
max
Firing Rate (Hz)
0
15 cm
Max: 10.55 Hz
Max: 14.52 Hz
Max: 10.54 Hz
Max: 6.04 Hz
Left trajectory
Right trajectory
Nosepoke
T Junction
Reward
Linearized Position on maze
Odor 1
Odor 2
Time from Odor Onset (s)
B
% of units with spatial fields
273
71
76
83
Odor Unresponsive
Odor Responsive
C
Rate during run (Hz)
Rate during odor (Hz)
D
Spatial Field Width (% of maze)
E
Absolute Association Selectivity Index
Non-traj. selective
Traj. selective
F
Trajectory Selectivity
Left
Right
Association Selectivity
G
Real Data
Shuffle
Decoding success probability
Track Quintile
H

Figure 5

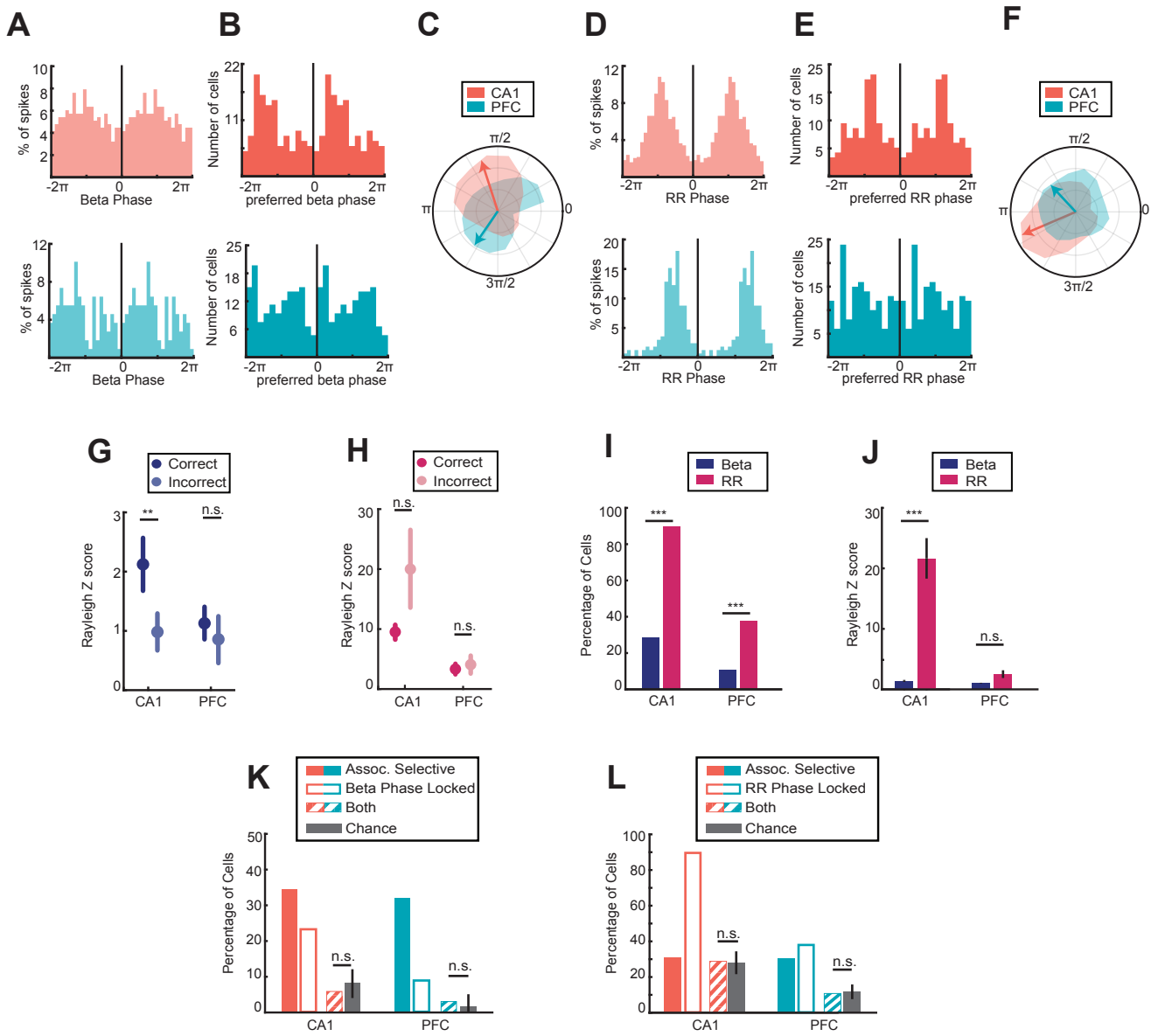
A
B
C
D
E
F
% of spikes
Beta Phase
Number of cells
preferred beta phase
CA1
PFC
π/2
π
0
3π/2
RR Phase
preferred RR phase
-2π
0
2π
G
H
I
J
Correct
Incorrect
Rayleigh Z score
Beta
RR
Percentage of Cells
**
***
n.s.
K
L
Assoc. Selective
Beta Phase Locked
RR Phase Locked
Both
Chance

Figure 6